# The elusive role of a deep-seated low-angle normal fault activated by the $M_w$ 9.0 Tohoku-Oki megathrust in the triggering of a normal faulting earthquake sequence in northeast Japan

Yohai Magen[1,2], Asaf Inbal[1], Alon Ziv[1], Gidon Baer[2], Roland Burgmann[3], Axel Periollat[4], and Takeshi Sagiya[5]

[1] Department of Geophysics, Tel-Aviv University, Tel Aviv, Israel

[2] Geological Survey of Israel, Jerusalem, Israel

[3]Department of Earth and Planetary Science, University of California Berkeley, Berkeley, CA, USA

[4] Univ. Grenoble Alpes, Univ. Savoie Mont Blanc, CNRS, IRD, Univ. Gustave Eiffel, ISTerre, 38000 Grenoble, France

[5] Disaster Mitigation Research Center, Nagoya University, Nagoya, Japan

Corresponding author: Yohai Magen (yohaimagen@mail.tau.ac.il)

Key Points:

- GNSS data analysis reveals a much larger aseismic than seismic strain in the Ibaraki-Fukushima Prefectural border
- The observed strain field resulted from transient slip on a blind low-angle normal fault offshore the study area
- Among on- and off-megathrust sources, the low angle normal fault is the primary source to static stress driving the Ibaraki-Fukushima swarm

## Abstract

Although deep-seated blind normal faults are common in subduction environments, their rheology, kinematics and interaction with the upper crust are poorly constrained. A month-long shallow normal faulting sequence in the Ibaraki-Fukushima prefectural border (IFPB), northeast Japan, which followed the $M_w$9.0 Tohoku-Oki earthquake (TOE) and culminated in the $M_w$6.7 Iwaki earthquake, provides a window into megathrust-to-normal fault interaction. Stress change calculations clearly indicate that the IFPB earthquake sequence cannot be explained in terms of direct triggering by the TOE co- and post-seismic slip. In quest for an alternative triggering mechanism, we analyzed post-TOE GNSS data from eastern IFPB. A key step in this analysis is the removal of the large-scale post TOE displacement field, after which a distinct highly-localized strain along the coastline becomes apparent. The accumulation of this strain was mostly aseismic, and migrated with time prior to the Iwaki earthquake in a manner that correlates well with post-TOE local seismicity. We attribute the pre-Iwaki earthquake strain accumulation to aseismic slip along low-angle seaward dipping blind normal fault, activated by the TOE. Stresses transferred by this slip episode accelerated the failure along the IFPB shallow normal faults. This indirect triggering of the Iwaki earthquake sequence by the TOE highlights the complexity of stress transfers in subduction environments.

## Plain Language Summary

The March 11th, 2011, Mw9.0 Tohoku-Oki megathrust earthquake (TOE) triggered widespread seismicity throughout north-east Japan. One of the most intense inland TOE aftershock sequences occurred along the Ibaraki-Fukushima Prefectural Border (IFPB) during the first month following the TOE. That sequence, which ended a long period of seismic quiescence in the IFPB area, culminated with the damaging April 11th, 2011, Mw6.7 Iwaki earthquake. The IFPB sequence is dominated by shallow normal faulting, suggesting regional extension. Due to its distance from the TOE slip area, activity in the IFPB cannot be explained solely due to the TOE co- or post-seismic slip. Here we analyze dense GNSS data and show that early post-seismic aseismic strain that accumulated in the IFPB greatly exceeded the seismic strain due to shallow normal faulting. We associate that strain with slip along a low-angle seaward dipping normal fault that is situated between the subduction interface and IFPB. We show that the low-angle normal fault's response to the TOE static stress change manifested in a month-long slip transient with an equivalent moment magnitude equal to Mw6.7. We find that slip along the low angle normal fault greatly enhances the failure of the shallow IFPB normal faults.


# 1. Introduction

Low angle faults cutting through the near-trench portion of the accretionary wedge are thought to play an important role in subduction seismogenesis (Park et al., 2002; Moore et al., 2007; Collot et al., 2008; Strasser et al., 2009) and in generating tsunamis (Baba et al., 2006; Wendt et al., 2009). Some deep-seated faults, however, cut through the portion of the inner forearc adjacent to the coastline (Plafker, 1965; Berryman et al., 2011; Clark et al., 2015). Those have been inferred to slip seismically with subduction earthquakes (Melnick et al., 2012) break during large immediate off-megathrust aftershocks (Berryman et al., 2011; Ryder et al., 2012) or time-advance as a result of stress transfer due to megathrust slip (Wiseman et al., 2011) Yet, the rheology of these deep-seated faults, and the fraction of the plate-boundary strain they accommodate, are poorly constrained. Not only is offshore faulting poorly resolved by on-land monitoring systems, offshore upper-plate fault slip histories are overwhelmed by inter-, co-, and postseismic slip occurring along the megathrust. Indeed, only rarely is the off-fault deformation field captured with sufficient spatio-temporal resolution, allowing one to document upper-plate faulting in action.

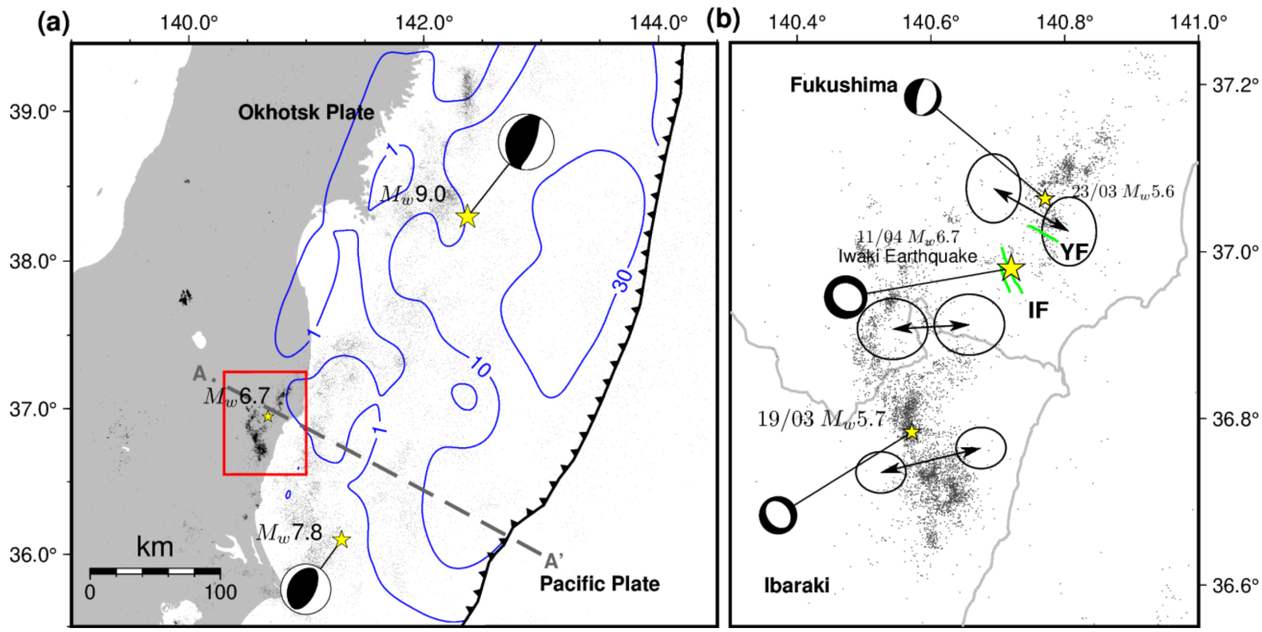


Figure 1. (a) The tectonic settings of northeast Japan. Yellow stars indicate the hypocenters of the March 11th, 2011, $M_w$9.0 TOE, the March 11th, 2011, $M_w$7.8 Ibaraki-Oki aftershock, and the April 11th, 2011, $M_w$6.7 Iwaki earthquakes. The blue contours show the TOE co-seismic slip distribution (Wei et al., 2012) with black dots representing aftershocks that occurred between March 11th and April 11th, 2011 (locations are from the JMA catalog). The dashed gray line indicates the A-A' depth cross-section shown in Figure 6, and the red rectangle indicates the IFPB region shown in panel b. (b) IFPB seismicity in the month following the TOE. The black lines with arrows on both ends indicate the direction of maximum tension inferred from focal mechanisms in the F-Net catalog compiled by the National Research Institute for Earth Science and Disaster Resilience (NIED), and the ellipses indicate the 95% confidence interval. The focal mechanisms of the three largest earthquakes were also taken from that catalog. The dark and light gray lines indicate the Japanese coast and the Ibaraki-Fukushima prefectural borderline, respectively. Green lines indicate the surface traces of faults ruptured during the April 11th, 2011 $M_w$6.7 Iwaki earthquake (Kobayashi et. al., 2012). Abbreviations: IF: Itozawa fault ; YF: Yunodake fault.

One such case is the March to April, 2011 seismic sequence in the IFPB, northeast Japan, which occurred shortly after the March 11, 2011, $M_w$9.0 TOE mainshock (Figure 1a). This giant earthquake altered the stress field in a region extending well beyond the ruptured fault area, as was manifested by intense seismic activity within the northeastern Japan forearc, as far as several hundreds of kilometers away from the epicenter (Hirose et al., 2011; Kato et al., 2011; Toda et al., 2011). Among the most intriguing post-TOE seismic sequences was the one recorded in the IFPB (Figure 1), where a long period of seismic quiescence came to an abrupt end (Abe, 1977; Kato et al., 2011; Imanishi et al., 2012; Toda and Tsutsumi, 2013). A vigorous earthquake sequence, which included 11 $M_w$>5 shallow normal-faulting earthquakes, struck the area within one month from the $M_w$9.0 mainshock. The sequence culminated with the $M_w$6.7 Iwaki earthquake, which ruptured a set of sub-parallel shallow normal faults in the Fukushima prefecture on April 11, 2011 (Imanishi et al., 2012; Kobayashi et al., 2012). Given the region's low strain rate (Mochizuki et al., 2008; Loveless and Meade, 2010), its distance from the trench, and its lack of volcanism, such an intense normal-faulting aftershock activity is puzzling. The modest Coulomb static stress change imparted by the $M_w$9.0 mainshock on IFPB (<1.5MPa ; Toda et al., 2011) appears to be too small to cause such an intense aftershock activity. Moreover, previous analyses of inter-seismic GPS velocity field (Mazzotti et al., 2001) and pre-TOE focal mechanisms (Townend and Zoback, 2006) imply that the IFPB is under E-W compression, thereby suggesting that the stress changes imposed by the TOE cannot overturn the long-term compressional stress field (Imanishi et al., 2012). Therefore it is difficult to associate IFPB's shallow normal faulting with trench-perpendicular extension induced by the $M_w$9.0 TOE (Kato et al., 2011; Yoshida et al., 2019).

Another mechanism that may explain the post-TOE IFPB anomalous seismic activity is transient deformation on a fault situated between the megathrust and eastern IFPB (Imanishi et al., 2012). According to this scenario, off-megathrust fault creep plays a role similar to the one played by moderate aftershocks, promoting long-range seismic fault interactions through multiple stress transfers (Felzer et al., 2002; Ziv, 2006; Inbal et al., 2017), an idea that is in line with the current understanding of earthquake interaction. Indeed, several independent evidences from tomographic (Shelly et al., 2006), magnetotelluric and geochemical studies (Umeda et al., 2015) support the existence of a deep-seated plane of discontinuity situated between the subduction interface and the IFPB. Unlike portions of the near-coast forearc to the north and south of Ibaraki, following the TOE, the volume surrounding that discontinuity hosted intense aftershock activity. Imanishi et al. (2012) proposed that the IFPB anomalous seismic activity was encouraged by off-megathrust fault slip occurring below the IFPB. That kind of deformation may be observed geodetically. However, isolating the signal due to slow post-TOE off-megathrust slip is complicated by the fact that the early post-TOE deformation field is dominated by megathrust afterslip, bulk visco-elastic relaxation, and aftershocks occurring along the megathrust and within the overriding plate.

The objective of this study is to uncover the causes for the post-TOE normal faulting sequence in the IFPB. In particular, we test whether the geodetic signal in the IFPB area can be attributed to slip along an off-megathrust structure located off-shore Ibaraki. To this end we analyze dense GNSS displacement data, and derive the strain field at the mid-points of GNSS site triplets. The switch from displacement to strain effectively screens out the regional deformation associated with post-TOE aseismic megathrust afterslip and bulk viscoelastic deformation, and reveals high concentration of local strain field in the IFPB area. This allows us to investigate the time-space evolution of the local strain field and the geodetic moment, and constrain the complex mechanism by which the TOE indirectly prompted normal faulting in the IFPB area.

# 2. Data and data processing

## 2.1. GNSS time series processing

To calculate the cumulative displacement in the IFPB region (Figure 2 and Figures S1, S2), during the interval between the TOE and the Iwaki earthquake, we used data from 59 GNSS Earth Observation Network System (GEONET) sites(Table S1), operated by the Geospatial Information Authority of Japan (Kato et al., 1998; Hatanaka et al., 2003; Sagiya, 2004). The GNSS time series, spanning the period between March 12$^{th}$, 2009, and April 11$^{th}$, 2011, were processed by the Nevada Geodetic Laboratory to generate daily station positions (Blewitt et al., 2018), relative to a fixed Pacific Plate coordinate system. To correct for long-term secular motion, semi-annual and annual motions, we implemented an iterative procedure to model daily position time-series of a two-year long interval preceding the TOE as (e.g., Williams, 2008; Montillet and Bos, 2019):

Equation 1.

$$x(t) = x_0 + a \cdot t + \sum_k \left[b_k \cos(2\pi/T_k) + c_k \sin(2\pi/T_k)\right] + n(t),$$

where $x_0$ is the initial location, $a$ is the secular velocity, $b_k$ and $c_k$ are the amplitudes of semi-annual and annual modulations with periods $T_k$ equal to 365.25 and 182.625 days, respectively, and $n(t)$ accounts for the measurement noise. We visually inspected these data to ensure they do not contain any significant transient tectonic-deformation signal. We then used the best-fitting coefficients to extrapolate the secular, semi-annual, and annual motions through the first month following the TOE, and removed the extrapolated values from these data. The post-processed displacement time-series are shown in Figure 2 and Figures S1-S2.

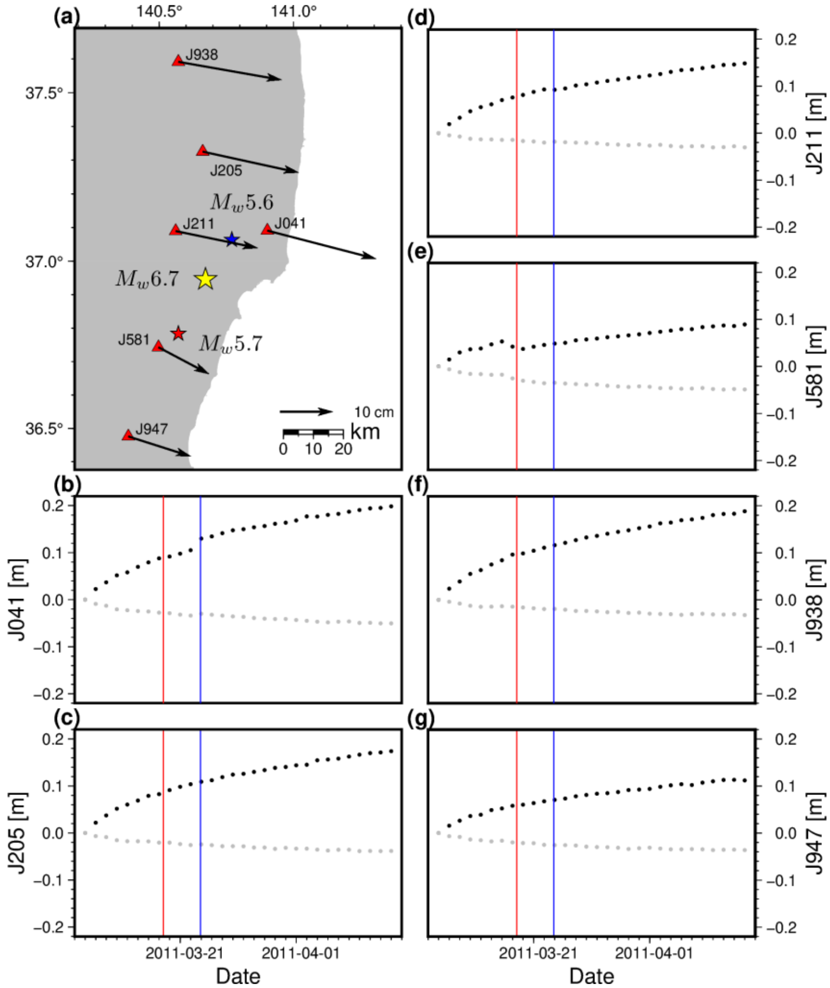


Figure 2. GNSS displacement data from 6 stations in the IFPB area. Data shown are after removal of secular, semi-annual, and annual terms (see stations details in Table S1). (a) Cumulative displacement between March 12 to April 10, 2011. Station locations are indicated by red triangles, location of $M_w$>5 earthquakes are shown with stars. (b)-(g) Displacement as a function of time. Black and gray dots indicate the east-west and north-south displacement, respectively. Red and blue vertical lines indicate the time of the March 19$^{th}$, 2011 $M_w$5.7 and March 23$^{rd}$, 2011 $M_w$5.6 earthquakes.

The post-processed displacement time-series include contributions from various sources. To examine the nature of these sources, it is useful to decompose the dataset to its spatial and temporal singular modes. To this end, the displacement time-series were arranged into a matrix, A, with $n$ rows corresponding to the number of GNSS stations, and $m$ columns corresponding to the number of days. Singular value decomposition (SVD) of A gives: $U\Sigma V^T$, with $U$ being an orthonormal matrix whose columns are the spatial eigenmodes, $V^T$, being an orthonormal matrix, whose rows are the temporal eigenmodes, and $\Sigma$ being a rectangular diagonal matrix of singular values. Following SVD, the i$^{th}$ singular component reads as: $u_i \sigma_i v_i^T$ , where $u_i$ and $v_i$ are the i$^{th}$ column of $U$ and $V$, respectively, and $\sigma_i$ is the i$^{th}$ singular value. The fraction of the data variance explained by the i$^{th}$ mode is calculated as:

Equation 2.

$$r_i^2 = \frac{\sigma_i^2}{\sum \sigma_j^2}$$

The result of the displacement SVD is presented in Figure 3a-c. The displacement data set decomposition indicates that more than 99.5 percent of the data are due to the first mode (Figure 3c). This mode exhibits large-scale temporal and spatial decays (Figure 3a-3b) that are attributable to the TOE postseismic slip and/or viscoelastic relaxation. This mode completely masks all other – smaller magnitude – local signals, and therefore hinders further investigation into the interaction between local aseismic and seismic slip.

### 2.2. Extracting the local aseismic strain field

To extract the local deformation from the large-scale regional geodetic deformation signal, we calculated the strain field common to neighboring GNSS sites. We used Delaunay triangulation to group the GNSS sites into triplets (Figure S1). The i$^{th}$ displacement component measured at location $y$ may be expressed as:

Equation 3.

$$x_i(y) = x_i(y_0) + \epsilon_{ij} dy_j + \omega_{ij} dy_j,$$

where $x_i(y_0)$ are the rigid-body translations between location $y_0$ and $y$, $\epsilon_{ij}$ is the infinitesimal strain tensor, $\omega_{ij}$ is the infinitesimal rigid-body rotation tensor, and $dy_j$ is the inter-station distance measured along direction $j$. Vertical displacement components were neglected, as interstation height differences are 2 to 3 orders of magnitude smaller than the horizontal distances, and therefore including them in the inversion leads to unstable results. The horizontal displacement data from each GNSS triplet may be used to formulate a set of equations for the translation, horizontal strain, and rotation. We solve this system of equations independently for each triplet and each day. The outputs are time-series containing the two horizontal rigid-body translations, the three independent components of the infinitesimal strain tensor, and the infinitesimal rotation representative of the polygon enclosed by the GNSS triplet.

The GNSS data contain noise which are mapped onto the calculated strains. Note that long-wavelength GNSS measurement errors, such as common-mode errors, are removed in the displacement-to-strain conversion step. To estimate strain uncertainties due to noise affecting the station triplets that was not removed during the differentiation, we take an empirical approach which relies on GNSS data recorded prior to the TOE. We calculated the strain accumulated in the IFPB region for 10000 randomly selected 1-30 day-long intervals extracted from the two years preceding the TOE. We assume that the total pre-TOE strain accumulating in the IFPB region during such short intervals is negligible, and use the pre-TOE strain uncertainties for estimating the uncertainties in the post-TOE strain time-series (see Supporting information for more details).

The effect of the displacement-to-strain conversion is illustrated by comparing the SVD spectra of the displacement time-series with that of the strain time-series. In contrast to the displacement data set, the strain data set is not dominated by any single mode. In fact, the first 7 modes together account for ~90 percent of the data (Figure 3f). Additionally, the cumulative effect of the first 7 spatial modes is highly localized in the IFPB region (Figure 3d). Thus, this analysis confirms that the displacement-to-strain conversion very effectively removes the large-scale deformation field. The sum of the first 7 temporal modes reveals two notable peaks, that are coeval with the March 19th $M_w$5.7 and the March 23rd $M_w$5.6 earthquakes (Figure 3e). Those earthquakes show notable offsets in the daily time series (Figure 2b and 2e), that are due to the combined effect of co- and post-seismic slip during each of these events.

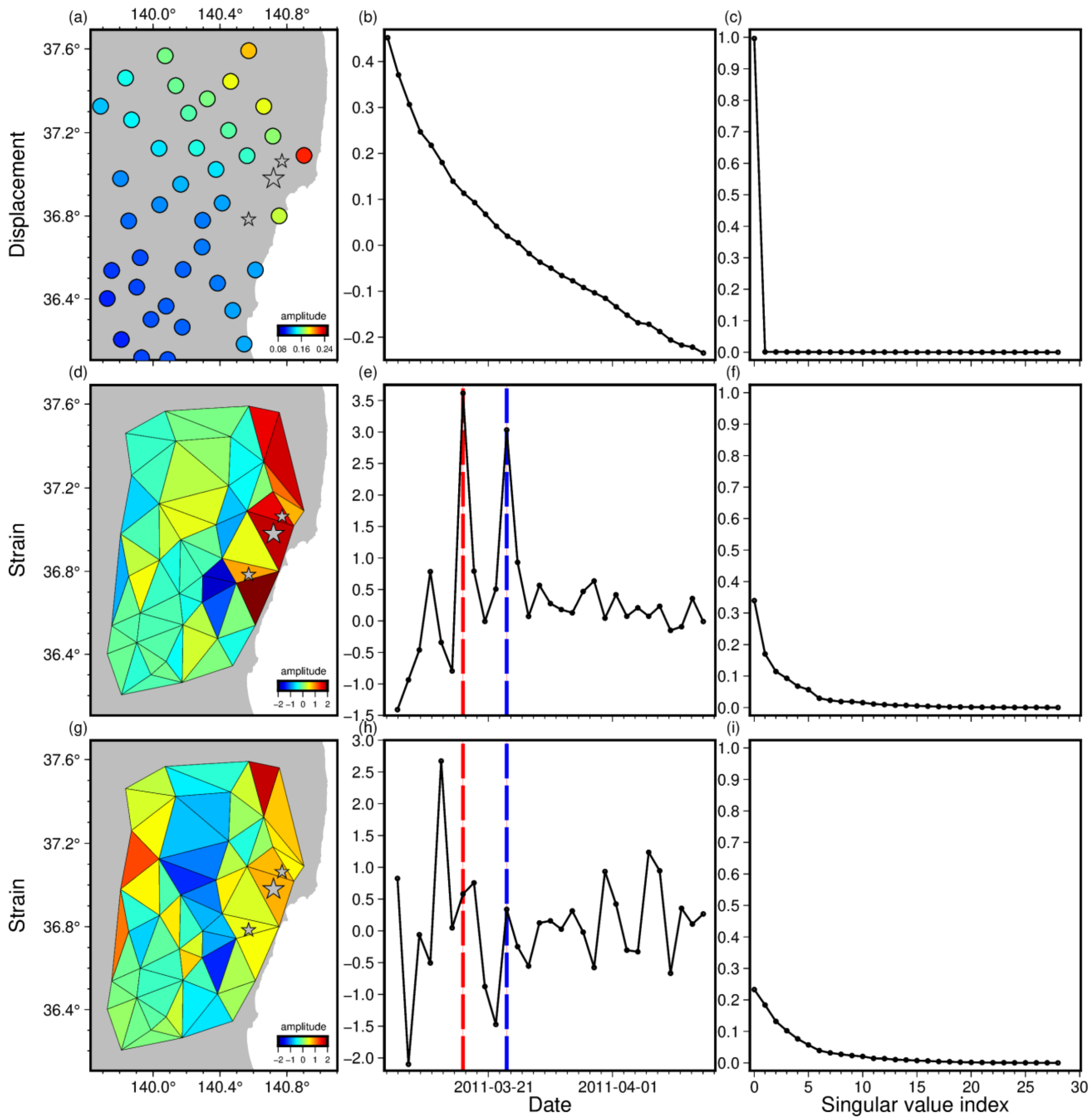


Figure 3. Comparison between the GNSS displacement and the inferred strain, and the effects of the March 19th and the March 23rd, 2011 earthquakes on the strain field. Stars are for earthquakes with Mw>5.5 that occurred between March 12th, 2011 and April 11th, 2011. The columns show the spatial mode of the data set (indicated by U), temporal mode of the data set (indicated by V), and the explained variance ratio of the singular values (Equation 2). (a) The displacement first spatial mode. The circles indicate the GNSS station locations, and the colors indicate the

amplitude of the reconstructed field from the eigen-modes. (b) The displacement first temporal mode. (c) The displacement singular values explained variance ratio. The first displacement mode accounts for more than 99% of the displacement variance. (d) The sum of the first seven strain spatial modes. Triangles indicate the locations of the GNSS triplets used to calculate the strain, and colors indicate the amplitude of the re-constructed field. (e) The sum of the first seven strain temporal modes (f) The strain singular values explained-variance ratio. The sum of the first seven strain modes accounts for ~90% of the strain data. (g) The sum of the first ten co-seismic free strain spatial modes. (h) The sum of the first ten coseismic-free strain temporal modes. (i) The coseismic-free strain singular values explained-variance ratio. The sum of the first ten coseismic-free strain modes accounts for ~90% of the coseismic-free strain data. Red and blue vertical lines in panels e and h indicate the times of the $M_w$5.7 March 19$^{th}$, 2011 and the $M_w$5.6 March 23$^{rd}$, 2011 earthquakes, respectively.

To remove the contribution of the coseismic offsets, we used sub-daily, 30-second GNSS time-series during the respective earthquakes (Periollat et al., 2022a; Periollat et al., 2022b). We used these solutions to subtract the coseismic offsets at stations surrounding the March 19$^{th}$ $M_w$5.7 and the March 23$^{rd}$ $M_w$5.6 earthquakes, with ten-minute time windows centered about the epoch of the events. We calculated the strain time-series of the seismic-free displacement data set. Inspection of the spatial and temporal eigenmodes of the seismic-free strain time-series indicates that the imprint of the co-seismic deformations due to the March 19$^{th}$ and 23$^{rd}$ earthquakes were largely removed from the strain data set (Figure 3g-3i). Inspection of the strain time-series and uncertainties confirms that the 5-day strain estimates are well above the daily strain noise level. In a later part, we use these strain time-series as input for the fault slip inversion procedure.

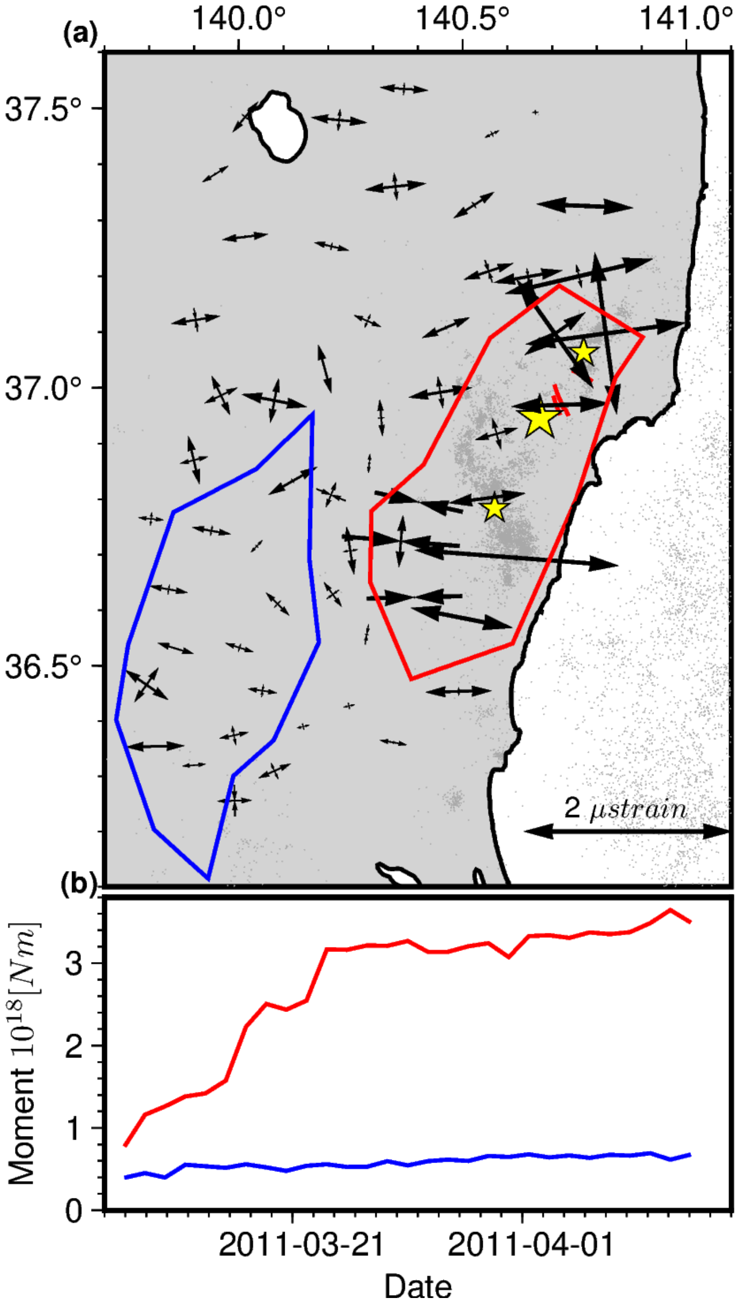


Figure 4. The IFPB strain field and moment accumulation. (a) Strain within the IFPB region accumulated between March $12^{th}$, 2011 and April $10^{th}$, 2011. Black arrows indicate the GNSS-inferred principal strains. Red and blue polygons indicate the IFPB and a reference region, respectively. The areal extent of the two regions is approximately equal (the IFPB areal extent is 2174 km$^2$ and the reference region's areal extent is 2223 km$^2$). (b) The geodetic moment accumulated between March $12^{th}$ to April $10^{th}$ up to 20 km depth. The red curve corresponds to the IFBP, and the blue curve corresponds to the reference region. The location of the two regions is shown in panel a.

# 3. Time-space evolution of the strain field and geodetic moment

The resolved geodetic strain is highly localized in the Ibaraki-Fukushima coastline, and its principal directions are consistent with the ones favoring the faulting observed during the March-April sequence (Figures 3 and 4). We find up to 20° orientation difference in the principal strain axis directions across the study area, with maximum extension changing from primarily east-west in the south near the March 19th earthquake hypocenter, to 108° east of north near the March 23rd earthquake hypocenter (Figure 5d). The principal strain directions and systematic rotation, which are also apparent in the seismologically-derived tension axes (Figure 1b), and the near-coast strain localization suggest that the observed IFPB strain field is not the result of slip along the subduction interface. To better understand the aseismic strain evolution and seismicity pattern in the IFPB, we examine the geodetic moment time-series. These were obtained using the approach of Savage and Simpson (1997), according to which the geodetic moment at a given volume is a function of the principal strains:

Equation 4.

$$M_0 = 2HA\mu(|\epsilon_1| + |\epsilon_2|),$$

where $\mu$ is the shear modulus, H is the crust thickness, assumed to be 20 km, A is the surface area covered by the GNSS triplets and $\epsilon_1$ and $\epsilon_2$ are the principal strains. We employed Equation 4 to calculate the daily geodetic moment during a 30-day-long time span starting on March 11th, 2011 (Figures 4 and 5). Additionally, we compared our geodetic moment calculation for the IFPB region with that of a similar size reference region (Figure 4). We found that between March 12th and April 10th, the geodetic moments in the reference and IFPB regions were $6.7 \cdot 10^{17} \pm 1.3 \cdot 10^{17}$ and $3.5 \cdot 10^{18} \pm 1.3 \cdot 10^{17}$ Nm, respectively.

The geodetic moment time-series reveal spatio-temporal variations in the rate of geodetic moment accumulation (Figure 5a). We observe rapid aseismic moment accumulation north and south of the Iwaki earthquake rupture, at rates that are initially higher than in the Iwaki earthquake area. The highest aseismic deformation rates are observed early in the sequence south of the Iwaki earthquake rupture area, and persist until March 19th. This deformation episode is associated with an increase in the rate of shallow microseismicity occurring both to the south and north of Iwaki earthquake (inset in Figure 5c), suggesting that the seismic activity there is being driven by aseismic fault slip. The deformation rates decreased around March 23rd. to a level that is nearly constant along the Ibaraki-Fukushima coast, but slightly larger in the Iwaki earthquake area than in adjacent areas. Similar to afterslip induced by large earthquakes, the accumulated moment exhibits a logarithmic dependence on time (Marone et al., 1991; Bürgmann et al., 1997; Hearn et al., 2002). Its temporal behavior is however complex, and is best described by the superposition of two logarithmic functions, with the first initiating on March 11th and the second on March 19th (Figure 5b). The absence of a large local earthquake in the IFPB on March 11th suggests that this uni- or bi-logarithmic moment accumulation resulted from interaction with an aseismically deforming structure.

The moment released aseismically in the IFPB during the first month following the TOE (Figure 5b) is about three times larger than that released seismically. The amplitude and distribution of the aseismic geodetic strain associated with this moment may neither be explained by shallow aseismic slip along the steep normal faults hosting the $M_w$>5 pre-Iwaki earthquake earthquakes (see section 4.3), nor by slip along the megathrust interface (Figures 3 and 4). Thus, in order to explain the excess strain in the IFPB, some unknown localized source of deformation should be considered. In the following section, we model the strain field and associate the source of deformation with a seaward dipping structure located off-shore the IFPB. We simultaneously solve for the structure's geometry and slip time-history, and show that the strains are consistent with transient slip along a low-angle normal fault underlying the eastern IFPB.

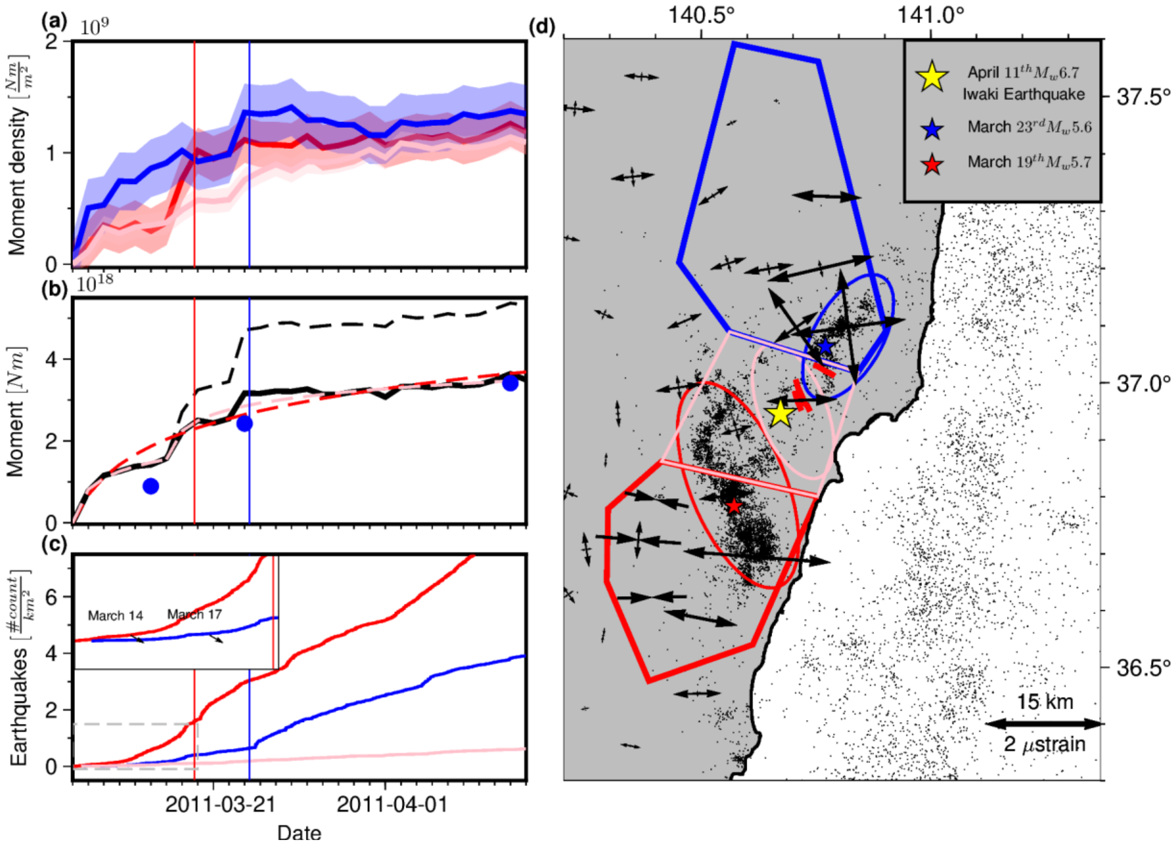


Figure 5. The temporal evolution of aseismic moment and seismicity in the IFPB area between March 12th and April 10th, 2011. Red and blue vertical lines indicate the times of the $M_w$5.7 and the $M_w$5.6 IFPB earthquakes. (a) The geodetic moment per area accumulated between March 12th, 2011, and April 10th, 2011. The colors correspond to the three polygons in panel d. Light colors indicate the 2-sigma confidence intervals around the mean. (b) The geodetic moment within the three polygons combined. The dashed and solid black curves represent the geodetic moment prior to and after the removal of the coseismic steps associated with the $M_w$5.7 and the $M_w$5.6 earthquakes. The red dashed line is for a model assuming moment accumulating logarithmically with time starting from March 12th, 2011, and the pink dashed curve is for a bi-logarithmic model, with the first starting on March 11th, 2011 and the second on March 19th, 2011. The blue circles indicate the moment calculated from the low-angle normal fault slip model (Figure 9). (c) The cumulative number of earthquakes with $M_w$>2 per area as a function of time. Curve colors correspond to the ellipses indicated in panel d. The black arrows and dates in the inset figure indicate the onset of seismicity rate acceleration (see discussion in Section

4.2). (d) Location map showing the polygons sub-dividing the IFBP. Strain within the IFPB coastline region accumulated between March 12th, 2011 and April 10th, 2011 is indicated by the black arrows.

# 4. Uncovering of a deep-seated low-angle normal fault and its triggering effect on the IFPB aftershock sequence

To uncover the source of elastic strain in the month preceding the Iwaki earthquake, we model the geodetic strain field. The assumption underlying our model is that the strain field in that area results mainly (but not solely) from slip along a single planar dislocation. In this section we invert the strains to obtain the dislocation geometry and slip distribution, and then examine the potential triggering effect that this source of deformation may have had on the normal faulting earthquake sequence in the IFPB area. We then compare the style of interaction between inverted dislocation and the shallow IFPB normal faulting sequence with previous models of IFPB fault interactions.

## 4.1. Fault geometry and slip inversion scheme

We perform a two-step fault slip inversion. In the first step we solve for the fault's location and geometry, and in the second step we solve for the fault's 2D slip distribution. We obtain the fault geometry by inverting the final horizontal strain distribution accumulated between March 12th and April 10th. Although the co-seismic offsets of the March 19th $M_w$5.7 and the March 23rd $M_w$5.6 earthquakes were already removed from the GNSS data, the strain still includes contributions from pre- or post-seismic slip occurring along the $M_w$5.6 and $M_w$5.7 faults. To account for this possibility, we simultaneously solve for the geometry (location, dimensions, strike, dip, and rake) and slip along a deep seated dislocation (Wright et al., 1999; Funning et al., 2005), as well as for the slips on a pair of shallow dislocations whose location and geometry were determined by previous studies of the $M_w$5.7 and $M_w$5.6 earthquakes (Kobayashi et al., 2012; Fukushima et al., 2018). We employ a Bayesian approach that uses a stochastic Monte Carlo Markov Chain (MCMC) procedure (Fukuda and Johnson, 2008; Minson et al., 2013), and construct a discrete view of the "true" probability density function (PDF). We allowed the dislocation geometry to vary freely, but constrained the slip direction to be in fault dip direction.

In the second step of the analysis, we inverted for distributed slip along a dislocation with a fixed geometry by setting the dislocation optimal geometry according to the mean expected value of $10^4$ MCMC iterations performed in the first step (Figure S4). We model the strain data using $n$ coplanar elastic dislocations representing the low-angle normal fault obtained in the first step. The slip inversion is set up to minimize the L2-norm of the differences between the observed and modeled strains:

Equation 5.

$$\|A \cdot m - \hat{\epsilon}\|_2 \rightarrow 0,$$

where $m$ is a vector that contains the output slip model, and $\hat{\epsilon}$ is a vector whose first n entries contain the observed strains and the remaining are set equal to zero. The matrix $A$ contains the elastic Green's functions (Okada, 1992) and smoothing kernel, and is written as:

Equation 6.

$$A = \begin{pmatrix} G \\ \beta \cdot \nabla \end{pmatrix},$$

where $G$ is the elastic kernel, $\nabla$ is a first-order derivative spatial operator, and $\beta$ is the smoothing coefficient. Equation 6 is solved by imposing non-negativity constraints on the slip model using the algorithm of Lawson and Hanson (1974).

## 4.2. Inversion results

The best fit slip distribution, fault geometry and location are presented in Figure 6. These results indicate that the strain concentration in the IFPB may be explained by creep along a blind low-angle normal fault located offshore. The optimal dislocation interface is dipping seaward at $25.7° \pm 13.7°$ with a strike of $28.4^o \pm 13^o$ and a dimension of $70.3 \pm 8.0$ by $61.6 \pm 8.0$ kilometers. Our slip distribution (Figure 6a) shows peak aseismic slip of up to 23 cm off-shore southern Fukushima over the first month following the TOE. The derived slip distribution fits the data reasonably well with a 52% residual variance reduction. The residuals variance reduction is increased to 65% when considering only GNSS triplets whose centers lie east of 140.3°, generally corresponding to triplets whose strain is well above the noise level (Figure S4). Our model suggests that the low-angle normal fault underlying the IFPB accumulated a geodetic moment equal to $2.6 \pm 1.3 \cdot 10^{19}$ Nm, equivalent to a moment magnitude equal to 6.7. Additionally, the moments we recover for the March 19$^{th}$ and March 23$^{rd}$ earthquakes faults are $3.4 \pm 1.4 \cdot 10^{17}$ and $2.8 \pm 3.0 \cdot 10^{16}$ Nm, respectively. The aseismic moment associated with the northern shallow fault was released after the March 23$^{rd}$ $M_w$5.6 earthquake, and its magnitude is equal to about 10% of the co-seismic moment of that earthquake (Kobayashi et al., 2012). In contrast, the aseismic moment near the southern shallow fault was released pre-seismically during the 3-4 days preceding the March 19$^{th}$ $M_w$5.7 earthquake (Figures 2e and Figure 6), and its magnitude is comparable to the coseismic moment of that earthquake.

The geometry we recover is consistent with previous studies, which proposed a large structure underlying the IFPB. Imanishi et al. (2012) analyzed the IFPB aftershock sequence, and concluded that the stresses imparted on the IFPB faults by the TOE mainshock were too small to activate the IFPB faults if pre-TOE compressional stresses had persisted in the IFPB area. They also noted that the distribution of hypocenters below ~10 km is localized off-shore the IFPB, without extending much to the north or to the south of the IFPB. To explain the anomalous IFPB activity and the clustering of deep (> 10 km) earthquakes off-shore IFPB, Imanishi et al. (2012) proposed that a seaward-dipping low-angel normal fault beneath the IFPB was activated due to stress imparted by the TOE. This structure also aligns with major discontinuities resolved in tomographic and magnetotelluric inversions (Shelly et al., 2006; Umeda et al., 2015; Zhao, 2015).

The on- and off-shore post-TOE hypocentral location and moment distributions are presented in Figure 7. Hypocenters occurring off the megathrust are found to cluster around the inferred low-angle normal fault plane, especially near the northern and southern edges of the fault, at depths between 20 to 30 km. The peak of seismic moment accumulated off-shore above the megathrust, shown in Figure 7g, also coincides with the location of the low-angle normal fault. The spatial clustering and seismic moment distribution suggest there is causal relationship between the low-angle normal fault slip and the aftershocks occurring above the megathrust. Note that we solve for the fault geometry that best fits the geodetically-derived surface strain data without imposing constraints (informed for example by the hypocentral distribution), and so the spatial correlation with seismicity lends further support to the inferred geometry. Also, note that the low-angle normal fault slip is generally larger at shallower depths than at deeper depths, a trend that is opposite to the one observed for the off-megathrust aftershocks, and which is consistent with the notion that the seismic to aseismic transition is controlled by a depth-dependent rheology. The complementarity between the aseismic slipping segment and intraplate seismic activity may have persisted long after the post-TOE first-month transient resolved here. Inspection of seismicity occurring between 2016 and 2022 in a catalog compiled using the Seafloor Observation Network for Earthquakes and Tsunamis (S-net, 2017) stations located offshore the IFPB reveals earthquake clustering in close proximity to low-angle normal fault plane (Figure S13). The near-low-angle fault earthquakes are mostly aftershocks of the November 2016 off-Fukushima $M_w$6.9 earthquake, which ruptured a low angle normal fault (Gusman et al., 2017; Kubota et al., 2021), located adjacent to the aseismic segment we found.

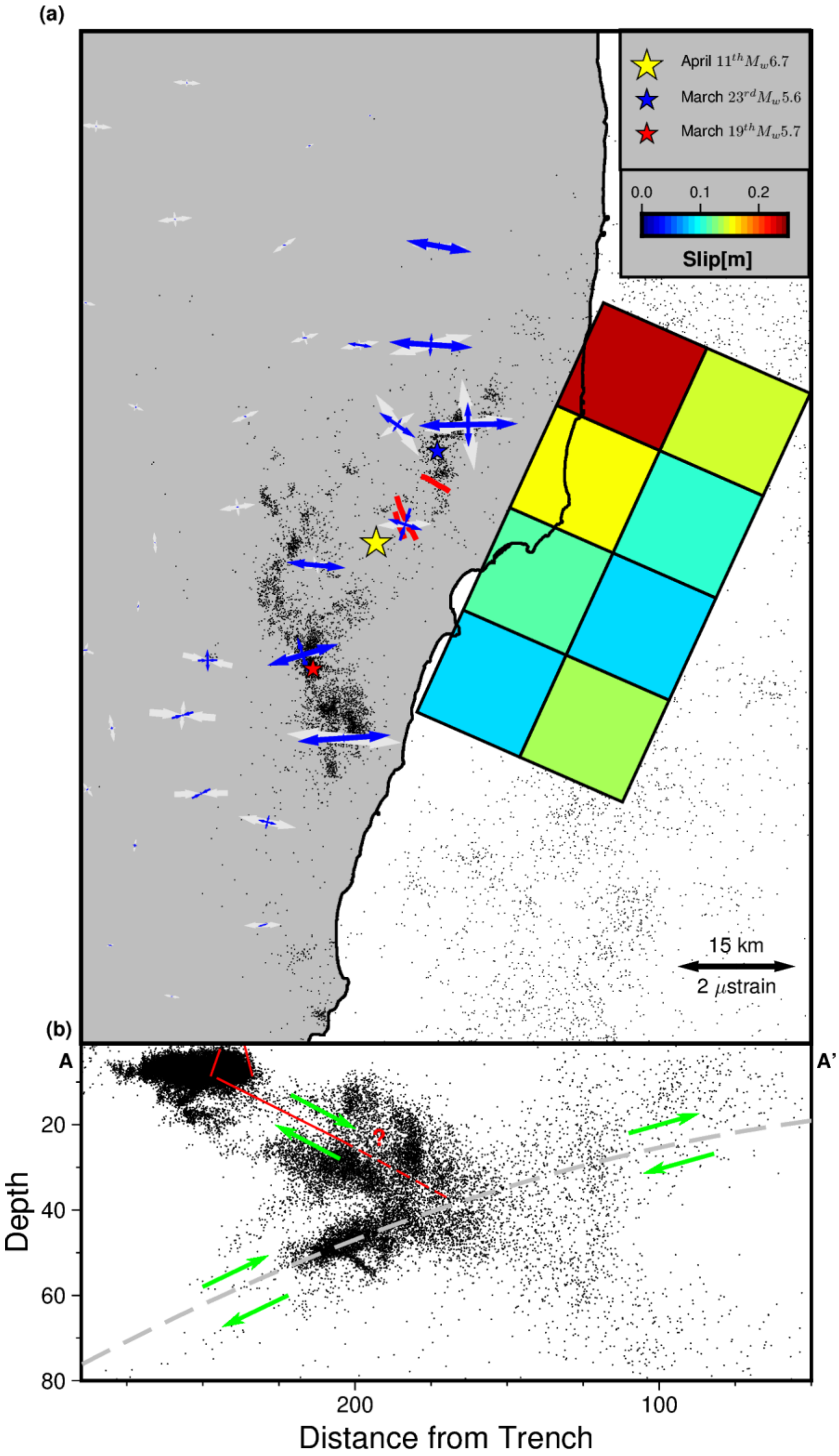


Figure 6. (a) The IFPB strain field inversion results. Modeled and observed principal strains are indicated by blue and light-gray arrows, respectively. The modeled low angle normal fault's surface projection is indicated by the black rectangle encompassing the cumulative slip distribution. Blue and red stars mark the epicenters of the March 19$^{th}$ 2011 $M_w$5.7, and the March 23$^{rd}$ 2011 $M_w$5.6 earthquakes, respectively. (b) Depth cross section of the IFPB region and the

offshore Japanese forearc with 1:3 vertical exaggeration. Black dots indicate aftershocks that occurred in the first month following the TOE mainshock within a strip extending out to 50 km on either side of the A-A' profile (see Figure 1a for location). The subduction interface (Hayes, 2018) is represented by a dashed gray line, and the low-angle normal fault and the shallow $M_w$>5.5 faults by the red lines. The sense of slip is indicated by the green arrows. The dashed red curve indicates the inferred geometry of the deep extent of the low angle normal fault, which is unresolved in our model.

## 4.3. Low-angle normal fault slip evolution and its triggering effect on the IFPB earthquake sequence

We calculate the Coulomb failure function (CFF) change imparted by the TOE on the low-angle normal fault according to: $\Delta\tau - \mu(\Delta\sigma_n - \Delta P)$, where $\Delta\tau$ is the shear stress change, $\mu$ is the friction coefficient, $\Delta\sigma_n$ is the normal stress change (positive in compression) and $\Delta P$ is the change in pore pressure. For computing the stress changes, we used Okada's dislocation equations (Okada, 1992) and the TOE slip distribution of Wei et al., (2012). Figure 8 presents the stress changes imposed by the TOE on the low-angle normal fault. The stress changes resolved on the low-angle normal fault vary between 0.4 and 1.2 MPa, thereby encouraging normal slip. The shallow stress change level increases toward the north, in a trend similar to the along-strike slip distribution at this depth range (Figure 6), such that the peak shallow slip and peak stress change are almost collocated.

Next, we examine the contributions of the TOE co-seismic slip and the low-angle normal fault slip to the stress field in the IFPB region. The results are presented in Figure 8, which shows the TOE- and low-angle normal fault induced extension in the IFPB area and the seismologically-derived principal horizontal tension directions (T-axis). The TOE peak extension is found to be an order of magnitude smaller than the low-angle normal fault slip induced extension in the IFPB area. Thus, the latter source is much more important for unclamping the IFPB shallow normal faults. In addition, whereas the TOE induces extension uniformly throughout the IFPB, the low-angle normal fault induced along-coast extension is localized near the IFPB faults, and especially near the northern seismicity cluster (blue ellipse in Figure 6) and two of the largest earthquakes in that sequence (the March 23, 2011 $M_w$5.6 and the April 11, 2011 $M_w$6.7 Iwaki earthquake; see Figure 8). We also find that the direction of maximum extension rotates by approximately 40$^o$, from 69° east of north in the southernmost section of the IFPB to 111° east of north in the northern section of the IFPB. The sense and amplitude of rotation of the modeled maximum extensions are similar to the ones inferred from the F-net moment tensor solution catalogue compiled by the National Research Institute for Earth Science and Disaster Prevention (NIED), and shown by the thin black arrows in Figure 8. On average, the moment tensors of the southern and northern IFPB seismicity clusters are associated with maximum extension oriented 76$^o$ and 111$^o$ east of north, respectively, within less than 20$^o$ of the observed strains in these two areas. The agreement between the geodetically-derived principal strains and seismically-derived tension axes indicate the aseismic and seismic deformations are likely the result of a common source, which is identified here with slip along the low-angle normal fault.

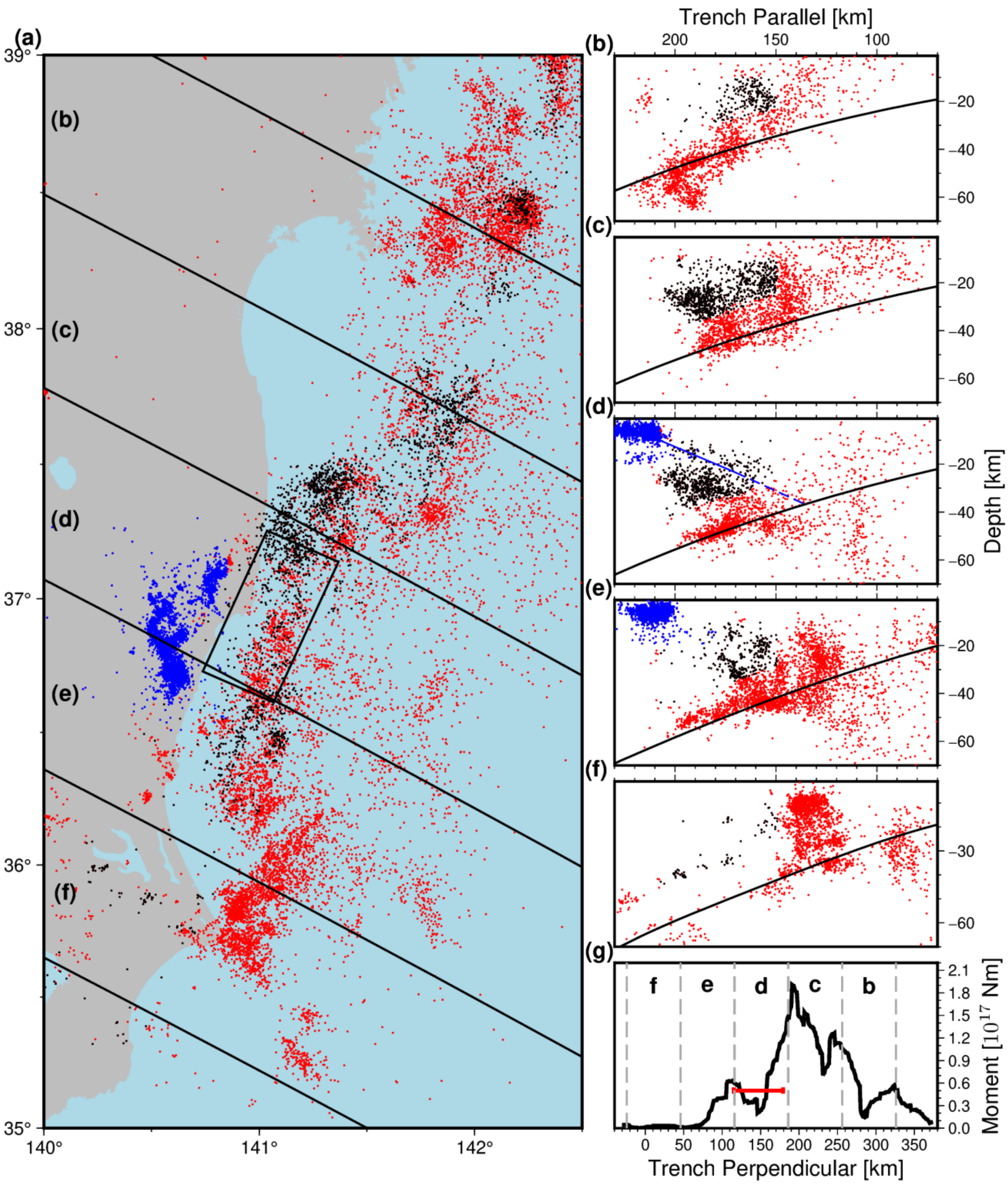


Figure 7. The distribution of $M_w$>2 earthquakes in northeast Japan between March 11th, 2011 and April 11th, 2011. Earthquakes were divided to three groups according to their location. Blue dots indicate primarily on-shore shallow seismicity associated with the IFPB sequence, red dots indicate off-shore events associated with the megathrust, and black dots indicate off-shore off-megathrust earthquakes occurring at depths larger than 20 km. The subduction geometry is from Hayes (2018). (a) Map view of the northeast Japan seismicity. Black lines indicate the location

of the trench-perpendicular profile presented in panels b-f. (b-f) Trench-perpendicular profiles corresponding to the locations in panel a. (g) Cumulative seismic moment of the off-shore off-megathrust seismicity (black dots in panels a-f). Gray dashed lines indicate the location of the profiles shown in panel (a) and red line indicates the location of the suggested low angle normal fault.

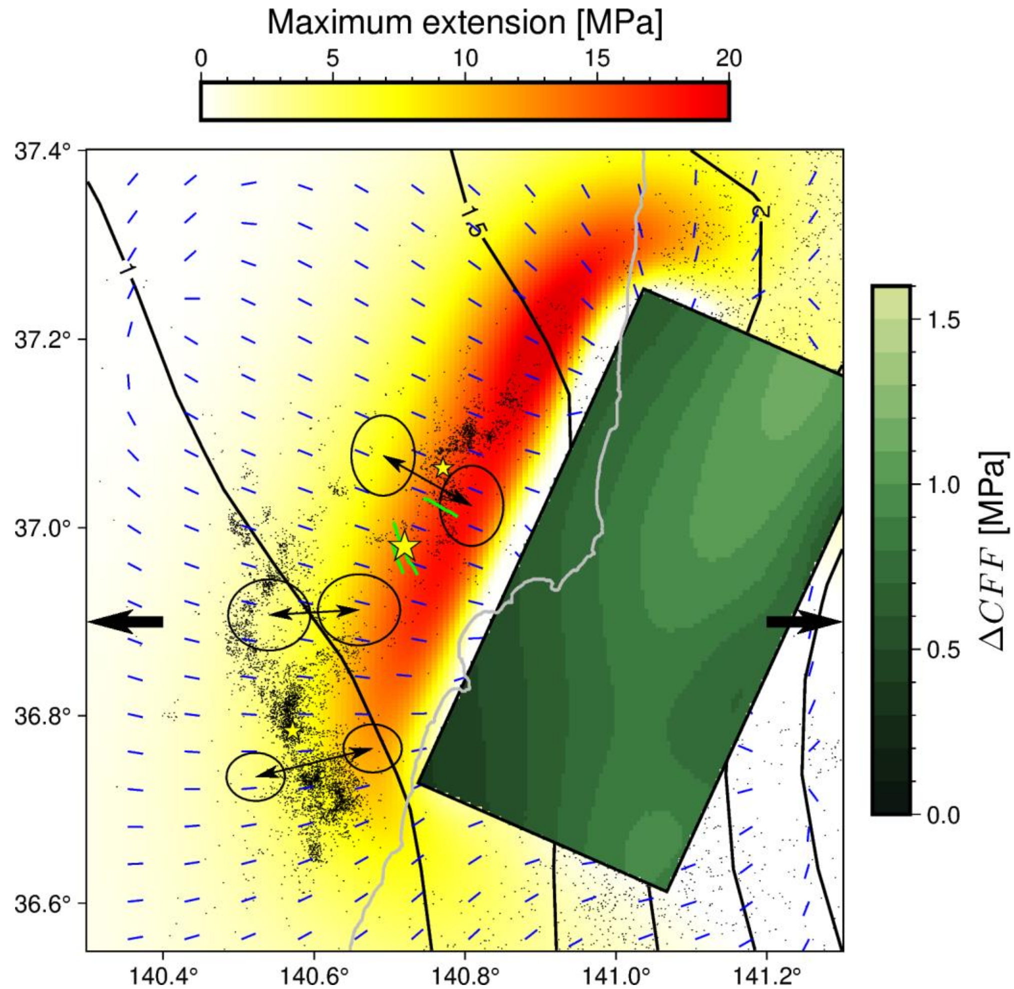


Figure 8. The stressing regime in the IFPB area following the TOE. The rectangle represents the low-angle normal fault and is colored according to the amplitude of the static CFF stress changes due to the TOE co-seismic slip (color scale at the right). The black contours and the thick black arrows indicate the magnitude and direction of the maximum extension induced by the TOE co-seismic slip at 5 km depth. The colors indicate the amplitude (color scale at the top) and thin blue lines indicate the direction of the maximum extension induced by slip along the low-angle normal fault. The thin black lines with arrows on both ends indicate the mean direction of maximum tension inferred from focal mechanisms in the F-net moment tensor solution catalogue compiled by the National Research Institute for Earth Science and Disaster Prevention (NIED), and the ellipses indicate the 95% confidence interval. Yellow stars show the location of $M_w$>5.5 earthquakes.

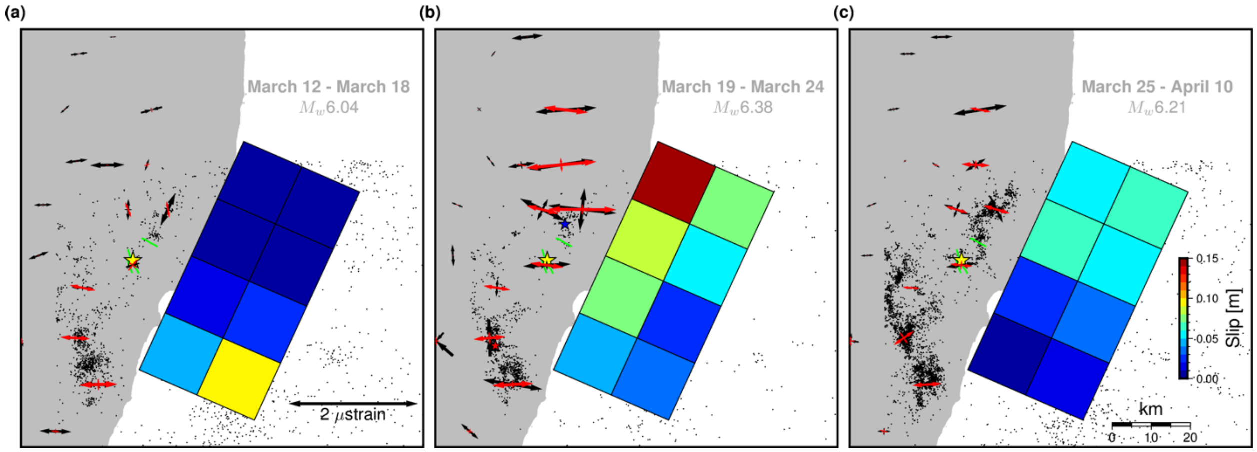


Figure 9. Snapshots of the low-angle normal fault slip distribution between March 12 to April 10, 2011. The intervals and equivalent moment magnitudes are indicated at the upper-right corner of each panel. Blue, red, and yellow stars are for the March 23rd $M_w$5.6, the March 19th $M_w$5.7, and the April 11th $M_w$6.7 Iwaki earthquakes, respectively. Green lines indicate the faults ruptured during the $M_w$6.7 Iwaki earthquake. Black dots indicate the location of seismicity that occurred during each time interval. (a) March 12th to March 18th. (b) March 19th to March 24th. (c) March 25 to April 10.

To further investigate the low-angle normal fault slip and stress field evolution in time and space, we inverted the slip distribution in three consecutive intervals as follows: March 12th to March 18th, March 19th to March 23rd, and March 24th to April 10th (blue circles in Figure 5b and Figure 9). We find that the slip transient migrated along the fault strike in a manner that correlates strongly with spatio-temporal evolution of the shallow seismicity in that area (Figure 5c inset). Prior to the March 19th $M_w$5.7 earthquake, slip on the low-angle normal fault occurred mainly around its southern section, directly to the east of the $M_w$5.7 fault, thereby increasing the CFF on that fault by 1.3 MPa. Between March 19th and March 23rd, slip migrated northward along-strike, where it was accommodated mostly along two fault patches located in the central and northern shallow part of the normal fault interface. Given the along-strike dimension, we estimate that the creep front propagated at a minimum average speed of 8-10 km/day, similar to the along-strike propagation speed of some slow slip events in Cascadia (Ghosh et al., 2010; Gomberg et al., 2010; Bartlow et al., 2011) and southwest Japan (Obara, 2002). Propagation at a similar rate is inferred from the local seismicity data, as is manifested by a 3-day delay in the onset of seismic activity between the northern Ibaraki to southern Fukushima sections (Figure 5c). Slip between March 19th and March 23rd increased the CFF on the fault hosting the March 23rd $M_w$5.6 southern Fukushima earthquake by about 10.3 MPa, thereby significantly promoting its failure. Between March 24 and April 10, slip occurred mainly along the central portion of the normal fault, directly to the east of the $M_w$6.7 Iwaki earthquake hypocenter, hence imparting unclamping stresses on the source region. We estimate that the fault, which broke during the $M_w$6.7 Iwaki earthquake, experienced about 7 MPa CFF change, 4.3 MPa due to slow normal fault slip between March 19th to March 23rd, and an additional 2.9 MPa due to slow normal fault slip in the central section until April 10th.

The total CFF imparted on the Iwaki earthquake faults by five deformation sources are compared in Figure 10. The deformation sources considered are: the TOE co-seismic (Wei et al., 2012) and post-seismic (Ozawa et al., 2011) slips, the $M_w$7.8 off Ibaraki-Oki subduction interface aftershock (Kubo et al., 2013), and the $M_w$5.7 and $M_w$5.6 shallow IFPB earthquakes (with slip as obtained from our inversion). This comparison indicates that the stress induced by the low-angle normal fault at the site of the Iwaki earthquake faults is by far the largest source of stress affecting those faults (Figure 8, 10). Furthermore, the 7 MPa total CFF imparted by the low-angle normal fault is notably larger than the 1.7 MPa median stress drop reported in Oth (2013) for intraplate earthquakes in Japan. We therefore conclude that the stress changes imparted by aseismic slip on the low-angle normal fault can be considered as the main source of stresses driving shallow normal faulting activity in the IFPB region.

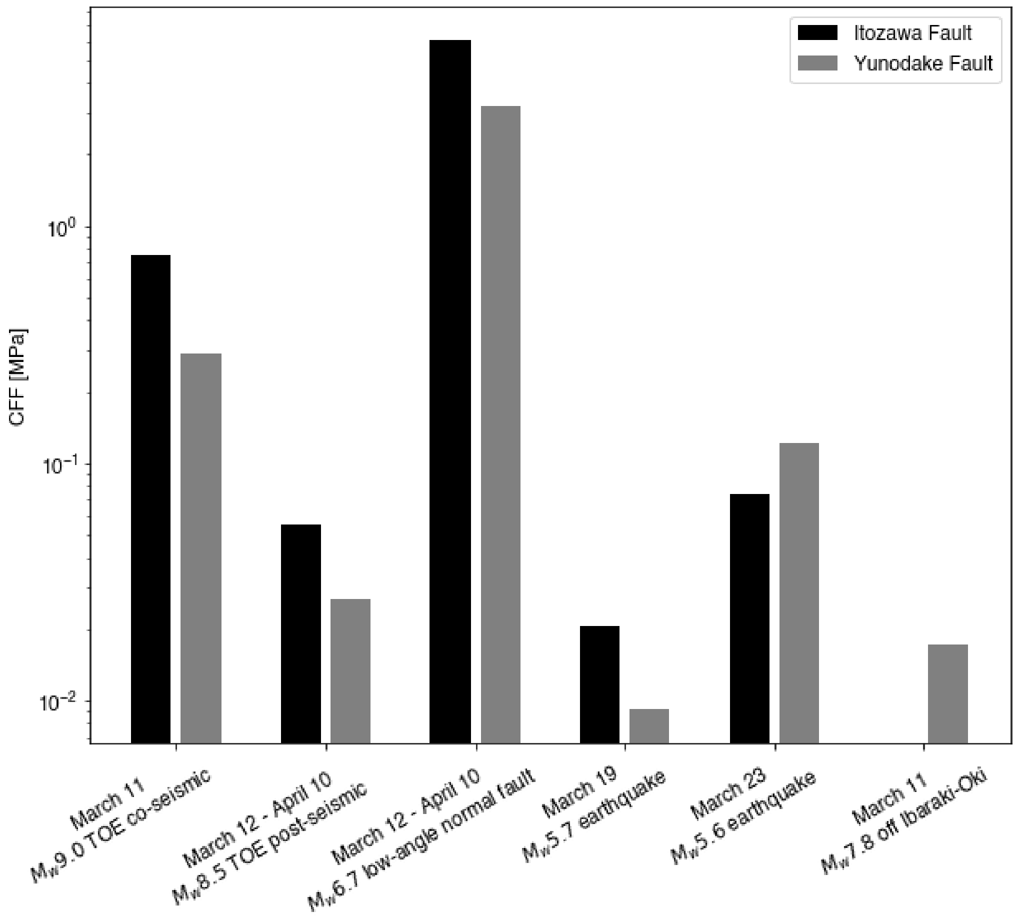


Figure 10. The CFF static stress change on the Itozawa and Yunodake $M_w$6.7 Iwaki earthquake faults (see Figure 1b for location). See main text for further details.

Shallow deformation rates in the IFPB area remained elevated long after the TOE, as was manifested by the occurrence of a $M_w$5.8 earthquake in the southern IFPB area on 2016, along the same fault associated with the March $19^{th}$, 2011, $M_w$5.7 earthquake. Fukushima et al. (2018) examined geodetic data, and proposed that significant post-seismic slip occurring after 2011 near the $M_w$5.7 source was responsible for shortening the recurrence interval between the $M_w$5.7 and

$M_w$5.8 southern IFPB earthquakes. Our inversion results are consistent with Fukushima et al. (2018)'s model, and suggest significant pre- and/or post-seismic slip on the southern IFPB $M_w$5.7 and $M_w$5.8 fault. Yet, slip along the low-angle fault plane seems to be important for explaining the geodetic dataset across the IFPB region. We found that removing the dislocation associated with the low angle normal fault from the model worsen the over-all fit to the data, resulting in a 30% decrease in the model's explained variance (Figure S8). Locally, however, Fukushima et al. (2018) model provides better fit to the data. Presumably, Fukushima et al. (2018) fit to the southern IFPB geodetic data is better than ours because they only used data near the 2011 $M_w$5.7 and 2016 $M_w$5.8 fault, and because they assumed a more complicated fault geometry. It is also possible that a mechanism similar to the one proposed by Fukushima et al. (2018) operated in the northern IFPB area, with contribution from afterslip following the March 23rd, 2011, $M_w$5.6 earthquake driving seismicity near the 2011 $M_w$5.6 source. Whereas some triggering around the $M_w$>5.5 faults may be ascribed to afterslip in vicinity of the rupture, that mechanism cannot explain the widespread distribution of post-TOE seismicity in the IFPB area, especially near the source of the $M_w$6.7 Iwaki earthquake, where evidence of afterslip is lacking. This conclusion is also supported by the observed temporal correlation between the low angle normal fault slip evolution and seismicity (Figure 7), and the correspondence between the geodetically-derived extension and seismologically-derived tension direction and sense of rotation (Figure 8). Other possible sources contributing to seismogenic behavior in the IFPB area may include the migration of lower-crustal fluids into the shallow crust, as indicated by the presence of low velocity zones beneath the study region (Kato et al., 2013; Umeda et al., 2015) and supported by geochemical evidence (Umeda et al., 2015). This process may be facilitated by permeability enhancement around the core of the low angle fault.

# 5. Implications of trench-parallel normal faulting offshore IFPB

The presence of a major deep-seated trench-parallel normal fault offshore IFPB implies a long-term trench-normal extensional regime in that area. Yet, the standard back-slip approach (Savage, 1983), with slab geometry, convergence rate and locking depth as in Suwa et al., (2006), yields inter-seismic CFF (using a friction coefficient that is equal to 0.4) rates on the low-angle normal fault of -12 to -1 KPa/yr, where the minus sign indicates stresses acting to discourage normal slip. Not only does this model implies an unfavorable stress regime for normal faulting offshore IFPB, it sets a threshold for triggering normal slip - namely, that the CFF induced by the TOE on the low-angle normal fault may be large enough to offset the negative CFF inferred from the back-slip model. That triggering threshold may be calculated if the repeat time of the TOE is known. Given that the previous megathrust earthquake on the TOE segment occurred 400 or more years ago (Uchida and Bürgmann, 2021), this result indicates a CFF threshold of 2.5 MPa. Thus, to offset the inter-seismic stress deficit requires either a ~1 MPa larger TOE stress change, or a larger pre-TOE CFF stress level on the low-angle normal fault. As the stress change imparted on the low-angle normal fault by the TOE is quite well-constrained, and only weakly sensitive to the details of the TOE near-trench slip distribution, we conclude that the pre-TOE stress acting on the low-angle normal fault must have been larger than the one predicted from the back-slip approach. It thus follows that the inter-seismic stress regime offshore IFPB is subject to additional stress inducing mechanisms, which operate to relieve the contraction imparted by the back-slip model.

This inference is also supported by seismological analysis of the November 2016 $M_w$6.9 off-Fukushima overriding plate normal-faulting earthquake, which ruptured a segment whose geometry is similar to the deep-seated aseismic low-angle normal fault resolved in this study. The seismic segment is located approximately along the deep-seated low-angle normal fault strike and to the north, manifesting a rheological transition in the off-Fukushima intraplate environment. Kobuta et al. (2021) used the dense S-net ocean-bottom network to obtain a source model for the 2016 $M_w$6.9, and found the $M_w$6.9 stress drop was considerably larger than the static stress change imparted by the TOE on the $M_w$6.9 source area. Based on this observation, and on seismological analysis suggesting horizontal extension prevailed in the overriding plate following the TOE (Asano et al., 2011; Hasegawa et al., 2012; Yoshida et al., 2012), Kobuta et al. (2021) suggested the overriding plate was under horizontal extension also before the TOE.

Extensional stress regime within the overriding plate may be the result of oceanward trench retreat, often referred to as trench rollback. This situation arises due to the negative buoyancy of the subducting plate relative to the surrounding mantle, when the vertical velocity of the downgoing slab exceeds the convergence rate (Garfunkel et al., 1986). Trench rollback is widespread along the western border of the Pacific plate (Sdrolias and Müller, 2006), and is believed to be responsible for the formation of some back-arc basins (Uyeda and Kanamori, 1979). This mechanism is thought to induce both contraction and extension within the overriding plate (Sdrolias and Müller, 2006), depending on the location relative to the trench. The distance over which the contraction, which prevails near the trench, transform to extension, is a function of the coupling, convergence rate, slab dip and along-strike curvature. Geodynamic models suggest that the transition occurs within 150 to 400 km landward of the trench (Capitanio et al., 2010), well within the range of the IFPB from the Japan trench. Indeed, previous studies suggest that the regional east-west contraction of northeast Japan induced by the subduction of the Pacific plate is non-uniform (Sagiya, 1999; Suwa et al., 2006; Loveless and Meade, 2010; Uchida and Matsuzawa, 2011). Focal mechanism solutions from the Ibaraki and Kanto coastline areas suggest that these areas underwent extension before the TOE (Imanishi et al., 2012; Yoshida et al., 2015; Hashima et al., 2020). This inference is also supported by paleoseismic data, indicating up to several meters of slip on the Iwaki earthquake faults during moderate-to-large normal-type earthquakes (Kobayashi et al., 2012; Toda and Tsutsumi, 2013; Miyashita, 2018). In summary, we conclude that the presence of a deep-seated trench-parallel normal fault offshore IFPB is consistent with recent geodynamic models of trench-rollback, with the inter-seismic focal mechanism analysis, and the shallow normal faulting in the adjacent coastline.

# 6. Summary and conclusions

The post-TOE earthquake sequence in the IFPB cannot be attributed solely to the stress modifications imparted by the co- and post-seismic slips of the TOE. To uncover the cause for this unusual seismic activity, we analyzed data recorded by a dense GNSS network. We showed that the post-TOE displacement field in eastern Japan is dominated by a large-scale eastward motion that decays with time and distance from the TOE. Focusing on the local deformation field within IFPB, we transformed the displacement field into strain field. The effect of this transformation is to remove the regional deformation due to the TOE postseismic relaxation process. The strain field is then used for the calculation of the geodetic moment within the IFPB crust volume, which indicates that the aseismic moment released in the IFPB area during the first month following the TOE was ten times larger than the seismic moment.

We suggest that the aseismic component of the deformation field was the result of a month-long slip transient on a deep-seated seaward dipping low-angle normal fault. The transient imparted a several-MPa static stress change on the Itozawa and Yunodake faults, ultimately leading to their failure, which resulted in the damaging $M_w$6.7 Iwaki earthquake. The inversion also indicates that slip migrated along the low-angle normal fault strike at a rate of 8 km/day, similar to the rate inferred from the local seismicity data. This correlation is manifested by a 3-day delay in the onset of seismic activity between the northern Ibaraki to southern Fukushima sections. Thus, aseismic and IFPB seismicity exhibit space-time correlations, highlighting the important role of stresses induced by low-angle normal fault slip in triggering that earthquake sequence.

The presence of such a major trench-parallel extensional structure offshore IFPB implies a long-term trench-normal extensional regime in that area. This extensional stress regime may be the result of a trench rollback. In summary, our spatio-temporal strain analysis and fault slip modeling strongly suggest that the TOE triggered a month-long aseismic slip transient on the low-angle normal fault, and that stresses induced by that slip transient encouraged normal faulting within IFPB. This mechanism explains the unusual post-TOE normal faulting sequence observed in that area.

# Open Research

The daily GNSS solutions can be obtained from the Nevada Geodetic Laboratory (Blewitt et al., 2018; refer to Table S1 for station IDs). For sub-daily GNSS solutions, the data from the GNSS kinematic position solutions in Japan is used (Periollat et al., 2022). The hypocentral catalog used in this study is provided by the Japan Meteorological Agency (Japan Meteorological Agency, 2024), and the moment tensor catalog is sourced from the National Research Institute for Earth Science and Disaster Resilience CMT solutions (NIED, 2024).The geometry of the Japanese subduction interface is based on the United States Geological Survey Uncertainty estimation for strain data (Hayes, 2018).

# References

Abe, K., 1977. Tectonic implications of the large shioya-oki earthquakes of 1938. Tectonophysics 41, 269–289. https://doi.org/10.1016/0040-1951(77)90136-6

Asano, Y., Saito, T., Ito, Y., Shiomi, K., Hirose, H., Matsumoto, T., Aoi, S., Hori, S., Sekiguchi, S., 2011. Spatial distribution and focal mechanisms of aftershocks of the 2011 off the Pacific coast of Tohoku Earthquake. Earth Planets Space 63, 669–673. https://doi.org/10.5047/eps.2011.06.016

Baba, T., Cummins, P.R., Hori, T., Kaneda, Y., 2006. High precision slip distribution of the 1944 Tonankai earthquake inferred from tsunami waveforms: Possible slip on a splay fault. Tectonophysics 426, 119–134. https://doi.org/10.1016/j.tecto.2006.02.015

Bartlow, N.M., Miyazaki, S., Bradley, A.M., Segall, P., 2011. Space-time correlation of slip and tremor during the 2009 Cascadia slow slip event. Geophys. Res. Lett. 38. https://doi.org/10.1029/2011GL048714

Berryman, K., Ota, Y., Miyauchi, T., Hull, A., Clark, K., Ishibashi, K., Iso, N., Litchfield, N., 2011. Holocene Paleoseismic History of Upper-Plate Faults in the Southern Hikurangi Subduction Margin, New Zealand, Deduced from Marine Terrace Records. Bull. Seismol. Soc. Am. 101, 2064–2087. https://doi.org/10.1785/0120100282

Blewitt, G., Hammond, W., Kreemer, C., 2018. Harnessing the GPS Data Explosion for Interdisciplinary Science. [Dataset]. Eos. https://doi.org/10.1029/2018eo104623

Bürgmann, R., Segall, P., Lisowski, M., Svarc, J., 1997. Postseismic strain following the 1989 Loma Prieta earthquake from GPS and leveling measurements. J. Geophys. Res. Solid Earth 102, 4933–4955. https://doi.org/10.1029/96JB03171

Capitanio, F.A., Stegman, D.R., Moresi, L.N., Sharples, W., 2010. Upper plate controls on deep subduction, trench migrations and deformations at convergent margins. Tectonophysics 483, 80–92. https://doi.org/10.1016/j.tecto.2009.08.020

Clark, K.J., Hayward, B.W., Cochran, U.A., Wallace, L.M., Power, W.L., Sabaa, A.T., 2015. Evidence for Past Subduction Earthquakes at a Plate Boundary with Widespread Upper Plate Faulting: Southern Hikurangi Margin, New Zealand. Bull. Seismol. Soc. Am. 105, 1661–1690. https://doi.org/10.1785/0120140291

Collot, J.-Y., Agudelo, W., Ribodetti, A., Marcaillou, B., 2008. Origin of a crustal splay fault and its relation to the seismogenic zone and underplating at the erosional north Ecuador–south Colombia oceanic margin. J. Geophys. Res. Solid Earth 113. https://doi.org/10.1029/2008JB005691

Felzer, K.R., Becker, T.W., Abercrombie, R.E., Ekström, G., Rice, J.R., 2002. Triggering of the 1999 MW 7.1 Hector Mine earthquake by aftershocks of the 1992 MW 7.3 Landers earthquake. J. Geophys. Res. Solid Earth 107, ESE 6-1-ESE 6-13. https://doi.org/10.1029/2001JB000911

Fukuda, J., Johnson, K.M., 2008. A fully Bayesian inversion for spatial distribution of fault slip with objective smoothing. Bull. Seismol. Soc. Am. https://doi.org/10.1785/0120070194

Fukushima, Y., Toda, S., Miura, S., Ishimura, D., Fukuda, J., Demachi, T., Tachibana, K., 2018. Extremely early recurrence of intraplate fault rupture following the Tohoku-Oki earthquake. Nat. Geosci. https://doi.org/10.1038/s41561-018-0201-x

Funning, G.J., Parsons, B., Wright, T.J., Jackson, J.A., Fielding, E.J., 2005. Surface displacements and source parameters of the 2003 Bam (Iran) earthquake from Envisat advanced synthetic aperture radar imagery. J. Geophys. Res. B Solid Earth 110, 1–23. https://doi.org/10.1029/2004JB003338

Garfunkel, Z., Anderson, C.A., Schubert, G., 1986. Mantle circulation and the lateral migration of subducted slabs. J. Geophys. Res. Solid Earth 91, 7205–7223. https://doi.org/10.1029/JB091iB07p07205

Ghosh, A., Vidale, J.E., Sweet, J.R., Creager, K.C., Wech, A.G., Houston, H., Brodsky, E.E., 2010. Rapid, continuous streaking of tremor in Cascadia. Geochem. Geophys. Geosystems 11. https://doi.org/10.1029/2010GC003305

Gomberg, J., the Cascadia 2007, Group, B.W., 2010. Slow-slip phenomena in Cascadia from 2007 and beyond: A review. GSA Bull. 122, 963–978. https://doi.org/10.1130/B30287.1

Gusman, A.R., Satake, K., Shinohara, M., Sakai, S., Tanioka, Y., 2017. Fault Slip Distribution of the 2016 Fukushima Earthquake Estimated from Tsunami Waveforms. Pure Appl. Geophys. 174, 2925–2943. https://doi.org/10.1007/s00024-017-1590-2

Hasegawa, A., Yoshida, K., Asano, Y., Okada, T., Iinuma, T., Ito, Y., 2012. Change in stress field after the 2011 great Tohoku-Oki earthquake. Earth Planet. Sci. Lett. 355–356, 231–243. https://doi.org/10.1016/j.epsl.2012.08.042

Hashima, A., Sato, H., Sato, T., 2020. Stress loading and the occurrence of normal-type earthquakes under Boso Peninsula, Japan. Earth Planets Space 72, 79. https://doi.org/10.1186/s40623-020-01201-6

Hatanaka, Y., Iizuka, T., Sawada, M., Yamagiwa, A., Kikuta, Y., Johnson, J.M., Rocken, C., 2003. Improvement of the analysis strategy of GEONET. Bull Geogr Surv Inst 49, 11–37.

Hayes, G., 2018. Slab2 - A Comprehensive Subduction Zone Geometry Model. [Dataset]. https://doi.org/10.5066/F7PV6JNV

Hearn, E.H., Bürgmann, R., Reilinger, R.E., 2002. Dynamics of İzmit Earthquake Postseismic Deformation and Loading of the Düzce Earthquake Hypocenter. Bull. Seismol. Soc. Am. 92, 172–193. https://doi.org/10.1785/0120000832

Hirose, F., Miyaoka, K., Hayashimoto, N., Yamazaki, T., Nakamura, M., 2011. Outline of the 2011 off the Pacific coast of Tohoku Earthquake (Mw 9.0) —Seismicity: foreshocks, mainshock, aftershocks, and induced activity—. Earth Planets Space 63, 1. https://doi.org/10.5047/eps.2011.05.019

Imanishi, K., Ando, R., Kuwahara, Y., 2012. Unusual shallow normal-faulting earthquake sequence in compressional northeast Japan activated after the 2011 off the Pacific coast of Tohoku earthquake. Geophys. Res. Lett. https://doi.org/10.1029/2012GL051491

Inbal, A., Ampuero, J.P., Avouac, J.P., 2017. Locally and remotely triggered aseismic slip on the central San Jacinto Fault near Anza, CA, from joint inversion of seismicity and strainmeter data. J. Geophys. Res. Solid Earth 122, 3033–3061. https://doi.org/10.1002/2016JB013499

Japan Meteorological Agency, 2024. Japan Meteorological Agency | The Seismological Bulletin of Japan . [Dataset]. Retrieved from https://www.data.jma.go.jp/eqev/data/bulletin/index_e.html.

Kato, A., Igarashi, T., Obara, K., Sakai, S., Takeda, T., Saiga, A., Iidaka, T., Iwasaki, T., Hirata, N., Goto, K., Miyamachi, H., Matsushima, T., Kubo, A., Katao, H., Yamanaka, Y., Terakawa, T., Nakamichi, H., Okuda, T., Horikawa, S., Tsumura, N., Umino, N., Okada, T., Kosuga, M., Takahashi, H., Yamada, T., 2013. Imaging the source regions of normal faulting sequences induced by the 2011 M9.0 Tohoku-Oki earthquake. Geophys. Res. Lett. 40, 273–278. https://doi.org/10.1002/grl.50104

Kato, A., Sakai, S., Obara, K., 2011. A normal-faulting seismic sequence triggered by the 2011 off the Pacific coast of Tohoku Earthquake: Wholesale stress regime changes in the upper plate. Earth Planets Space 63, 43. https://doi.org/10.5047/eps.2011.06.014

Kato, T., El-Fiky, G.S., Oware, E.N., Miyazaki, S., 1998. Crustal strains in the Japanese Islands as deduced from dense GPS array. Geophys. Res. Lett. 25, 3445–3448. https://doi.org/10.1029/98GL02693

Kobayashi, T., Tobita, M., Koarai, M., Okatani, T., Suzuki, A., Noguchi, Y., Yamanaka, M., Miyahara, B., 2012. InSAR-derived crustal deformation and fault models of normal faulting earthquake (mj 7.0) in the fukushima-hamadori area. Earth Planets Space. https://doi.org/10.5047/eps.2012.08.015

Kubo, H., Asano, K., Iwata, T., 2013. Source-rupture process of the 2011 Ibaraki-oki, Japan, earthquake (Mw 7.9) estimated from the joint inversion of strong-motion and GPS Data: Relationship with seamount and Philippine Sea Plate. Geophys. Res. Lett. 40, 3003–3007. https://doi.org/10.1002/grl.50558

Kubota, T., Kubo, H., Yoshida, K., Chikasada, N.Y., Suzuki, W., Nakamura, T., Tsushima, H., 2021. Improving the Constraint on the Mw 7.1 2016 Off-Fukushima Shallow Normal-Faulting Earthquake With the High Azimuthal Coverage Tsunami Data From the S-Net Wide and Dense Network: Implication for the Stress Regime in the Tohoku Overriding Plate. J. Geophys. Res. Solid Earth 126, e2021JB022223. https://doi.org/10.1029/2021JB022223

Lawson, C.L., Hanson, R.J., 1974. Solving Least-Squares Problems, in: Solving Least-Squares Problems. https://doi.org/10.3141/1671-03

Loveless, J.P., Meade, B.J., 2010. Geodetic imaging of plate motions, slip rates, and partitioning of deformation in Japan. J. Geophys. Res. Solid Earth 115. https://doi.org/10.1029/2008JB006248

Marone, C.J., Scholtz, C.H., Bilham, R., 1991. On the mechanics of earthquake afterslip. J. Geophys. Res. Solid Earth 96, 8441–8452. https://doi.org/10.1029/91JB00275

Mazzotti, S., Henry, P., Le Pichon, X., 2001. Transient and permanent deformation of central Japan estimated by GPS: 2. Strain partitioning and arc–arc collision. Earth Planet. Sci. Lett. 184, 455–469. https://doi.org/10.1016/S0012-821X(00)00336-8

Melnick, D., Moreno, M., Motagh, M., Cisternas, M., Wesson, R.L., 2012. Splay fault slip during the Mw 8.8 2010 Maule Chile earthquake. Geology 40, 251–254. https://doi.org/10.1130/G32712.1

Minson, S.E., Simons, M., Beck, J.L., 2013. Bayesian inversion for finite fault earthquake source models I-theory and algorithm. Geophys. J. Int. https://doi.org/10.1093/gji/ggt180

Miyashita, Y., 2018. Holocene paleoseismic history of the Yunodake fault ruptured by the 2011 Fukushima-ken Hamadori earthquake, Fukushima Prefecture, Japan. Geomorphology 323, 70–79. https://doi.org/10.1016/J.GEOMORPH.2018.08.040

Mochizuki, K., Yamada, T., Shinohara, M., Yamanaka, Y., Kanazawa, T., 2008. Weak Interplate Coupling by Seamounts and Repeating *M* ~ 7 Earthquakes. Science 321, 1194–1197. https://doi.org/10.1126/science.1160250

Montillet, J.-P., Bos, M.S., 2019. Geodetic time series analysis in earth sciences. Springer.

Moore, G.F., Bangs, N.L., Taira, A., Kuramoto, S., Pangborn, E., Tobin, H.J., 2007. Three-Dimensional Splay Fault Geometry and Implications for Tsunami Generation. Science 318, 1128–1131. https://doi.org/10.1126/science.1147195

NIED, 2024. National Research Institute for Earth Science and Disaster Resilience | F-net Moment Tensors catalog. [Dataset]. Retrieved from https://www.fnet.bosai.go.jp/event/search.php?LANG=en.

Obara, K., 2002. Nonvolcanic Deep Tremor Associated with Subduction in Southwest Japan. Science 296, 1679–1681. https://doi.org/10.1126/science.1070378

Okada, Y., 1992. Internal deformation due to shear and tensile faults in a half-space. Bull. - Seismol. Soc. Am.

Oth, A., 2013. On the characteristics of earthquake stress release variations in Japan. Earth Planet. Sci. Lett. 377–378, 132–141. https://doi.org/10.1016/j.epsl.2013.06.037

Ozawa, S., Nishimura, T., Suito, H., Kobayashi, T., Tobita, M., Imakiire, T., 2011. Coseismic and postseismic slip of the 2011 magnitude-9 Tohoku-Oki earthquake. Nature. https://doi.org/10.1038/nature10227

Park, J.-O., Tsuru, T., Kodaira, S., Cummins, P.R., Kaneda, Y., 2002. Splay Fault Branching Along the Nankai Subduction Zone. Science 297, 1157–1160. https://doi.org/10.1126/science.1074111

Periollat, Axel, Radiguet, M., Weiss, J., Twardzik, C., Amitrano, D., Cotte, N., Marill, L., Socquet, A., 2022. Transient Brittle Creep Mechanism Explains Early Postseismic Phase of the 2011 Tohoku-Oki Megathrust Earthquake: Observations by High-Rate GPS Solutions. J. Geophys. Res. Solid Earth 127, e2022JB024005. https://doi.org/10.1029/2022JB024005

Periollat, A., Twardzik, C., Cotte, N., Radiguet, M., Socquet, A., Marill, L., 2022. GNSS kinematic position solutions in Japan. These Datasets Provide GNSS Solut. Contin. Stn. Jpn. Data Come GNSS Earth Obs. Netw. Syst. Jpn. GEONET. [Dataset]. https://doi.org/10.17178/GNSS.PRODUCTS.JAPAN_GIPSYX.KINEMATIC.2011

Plafker, G., 1965. Tectonic Deformation Associated with the 1964 Alaska Earthquake. Science 148, 1675–1687. https://doi.org/10.1126/science.148.3678.1675

Ryder, I., Rietbrock, A., Kelson, K., Bürgmann, R., Floyd, M., Socquet, A., Vigny, C., Carrizo, D., 2012. Large extensional aftershocks in the continental forearc triggered by the 2010 Maule earthquake, Chile. Geophys. J. Int. 188, 879–890. https://doi.org/10.1111/j.1365-246X.2011.05321.x

Sagiya, T., 2004. A decade of GEONET: 1994-2003 - The continuous GPS observation in Japan and its impact on earthquake studies -. Earth Planets Space. https://doi.org/10.1186/BF03353077

Sagiya, T., 1999. Interplate coupling in the Tokai District, central Japan, deduced from continuous GPS data. Geophys. Res. Lett. 26, 2315–2318. https://doi.org/10.1029/1999GL900511

Savage, J.C., 1983. A dislocation model of strain accumulation and release at a subduction zone. J. Geophys. Res. Solid Earth 88, 4984–4996. https://doi.org/10.1029/JB088iB06p04984

Savage, J.C., Simpson, R.W., 1997. Surface strain accumulation and the seismic moment tensor. Bull. Seismol. Soc. Am.

Sdrolias, M., Müller, R.D., 2006. Controls on back-arc basin formation. Geochem. Geophys. Geosystems 7. https://doi.org/10.1029/2005GC001090

Shelly, D.R., Beroza, G.C., Zhang, H., Thurber, C.H., Ide, S., 2006. High-resolution subduction zone seismicity and velocity structure beneath Ibaraki Prefecture, Japan. J. Geophys. Res. Solid Earth 111. https://doi.org/10.1029/2005JB004081

S-net, N., 2017. National Research Institute for Earth Science "and Disaster Resiliences S-net. https://doi.org/10.17598/NIED.0007

Strasser, M., Moore, G.F., Kimura, G., Kitamura, Y., Kopf, A.J., Lallemant, S., Park, J.-O., Screaton, E.J., Su, X., Underwood, M.B., Zhao, X., 2009. Origin and evolution of a splay fault in the Nankai accretionary wedge. Nat. Geosci. 2, 648–652. https://doi.org/10.1038/ngeo609

Suwa, Y., Miura, S., Hasegawa, A., Sato, T., Tachibana, K., 2006. Interplate coupling beneath NE Japan inferred from three-dimensional displacement field. J. Geophys. Res. Solid Earth 111. https://doi.org/10.1029/2004JB003203

Toda, S., Stein, R.S., Lin, J., 2011. Widespread seismicity excitation throughout central Japan following the 2011 M=9.0 Tohoku earthquake and its interpretation by Coulomb stress transfer. Geophys. Res. Lett. 38. https://doi.org/10.1029/2011GL047834

Toda, S., Tsutsumi, H., 2013. Simultaneous Reactivation of Two, Subparallel, Inland Normal Faults during the Mw 6.6 11 April 2011 Iwaki Earthquake Triggered by the Mw 9.0 Tohoku-oki, Japan, EarthquakeSimultaneous Reactivation of Two Normal Faults during Iwaki Earthquake Triggered by T. Bull. Seismol. Soc. Am. 103, 1584–1602. https://doi.org/10.1785/0120120281

Townend, J., Zoback, M.D., 2006. Stress, strain, and mountain building in central Japan. J. Geophys. Res. Solid Earth 111. https://doi.org/10.1029/2005JB003759

Uchida, N., Bürgmann, R., 2021. A Decade of Lessons Learned from the 2011 Tohoku-Oki Earthquake. Rev. Geophys. 59, e2020RG000713. https://doi.org/10.1029/2020RG000713

Uchida, N., Matsuzawa, T., 2011. Coupling coefficient, hierarchical structure, and earthquake cycle for the source area of the 2011 off the Pacific coast of Tohoku earthquake inferred from small repeating earthquake data. Earth Planets Space 2011 637 63, 675–679. https://doi.org/10.5047/EPS.2011.07.006

Umeda, K., Asamori, K., Makuuchi, A., Kobori, K., Hama, Y., 2015. Triggering of earthquake swarms following the 2011 Tohoku megathrust earthquake. J. Geophys. Res. Solid Earth 120, 2279–2291. https://doi.org/10.1002/2014JB011598

Uyeda, S., Kanamori, H., 1979. Back-arc opening and the mode of subduction. J. Geophys. Res. Solid Earth 84, 1049–1061. https://doi.org/10.1029/JB084iB03p01049

Wei, S., Graves, R., Helmberger, D., Avouac, J.-P., Jiang, J., 2012. Sources of shaking and flooding during the Tohoku-Oki earthquake: A mixture of rupture styles. Earth Planet. Sci. Lett. 333–334, 91–100. https://doi.org/10.1016/j.epsl.2012.04.006

Wendt, J., Oglesby, D.D., Geist, E.L., 2009. Tsunamis and splay fault dynamics. Geophys. Res. Lett. 36. https://doi.org/10.1029/2009GL038295

Williams, S.D.P., 2008. CATS: GPS coordinate time series analysis software. GPS Solut. 2007 122 12, 147–153. https://doi.org/10.1007/S10291-007-0086-4

Wiseman, K., Banerjee, P., Sieh, K., Bürgmann, R., Natawidjaja, D.H., 2011. Another potential source of destructive earthquakes and tsunami offshore of Sumatra. Geophys. Res. Lett. 38. https://doi.org/10.1029/2011GL047226

Wright, T.J., Parsons, B.E., Jackson, J.A., Haynes, M., Fielding, E.J., England, P.C., Clarke, P.J., 1999. Source parameters of the 1 October 1995 Dinar (Turkey) earthquake from SAR interferometry and seismic bodywave modelling. Earth Planet. Sci. Lett. 172, 23–37. https://doi.org/10.1016/S0012-821X(99)00186-7

Yoshida, K., Hasegawa, A., Okada, T., 2015. Spatially heterogeneous stress field in the source area of the 2011 Mw 6.6 Fukushima-Hamadori earthquake, NE Japan, probably caused by static stress change. Geophys. J. Int. 201, 1062–1071. https://doi.org/10.1093/gji/ggv068

Yoshida, K., Hasegawa, A., Okada, T., Iinuma, T., Ito, Y., Asano, Y., 2012. Stress before and after the 2011 great Tohoku-oki earthquake and induced earthquakes in inland areas of eastern Japan. Geophys. Res. Lett. 39. https://doi.org/10.1029/2011GL049729

Yoshida, K., Hasegawa, A., Yoshida, T., Matsuzawa, T., 2019. Heterogeneities in Stress and Strength in Tohoku and Its Relationship with Earthquake Sequences Triggered by the 2011 M9 Tohoku-Oki Earthquake. Pure Appl. Geophys. 176, 1335–1355. https://doi.org/10.1007/s00024-018-2073-9

Zhao, D., 2015. The 2011 Tohoku earthquake (Mw 9.0) sequence and subduction dynamics in Western Pacific and East Asia. J. Asian Earth Sci. 98, 26–49. https://doi.org/10.1016/j.jseaes.2014.10.022

Ziv, A., 2006. On the Role of Multiple Interactions in Remote Aftershock Triggering: The Landers and the Hector Mine Case Studies. Bull. Seismol. Soc. Am. 96, 80–89. https://doi.org/10.1785/0120050029

**Figure 1.**

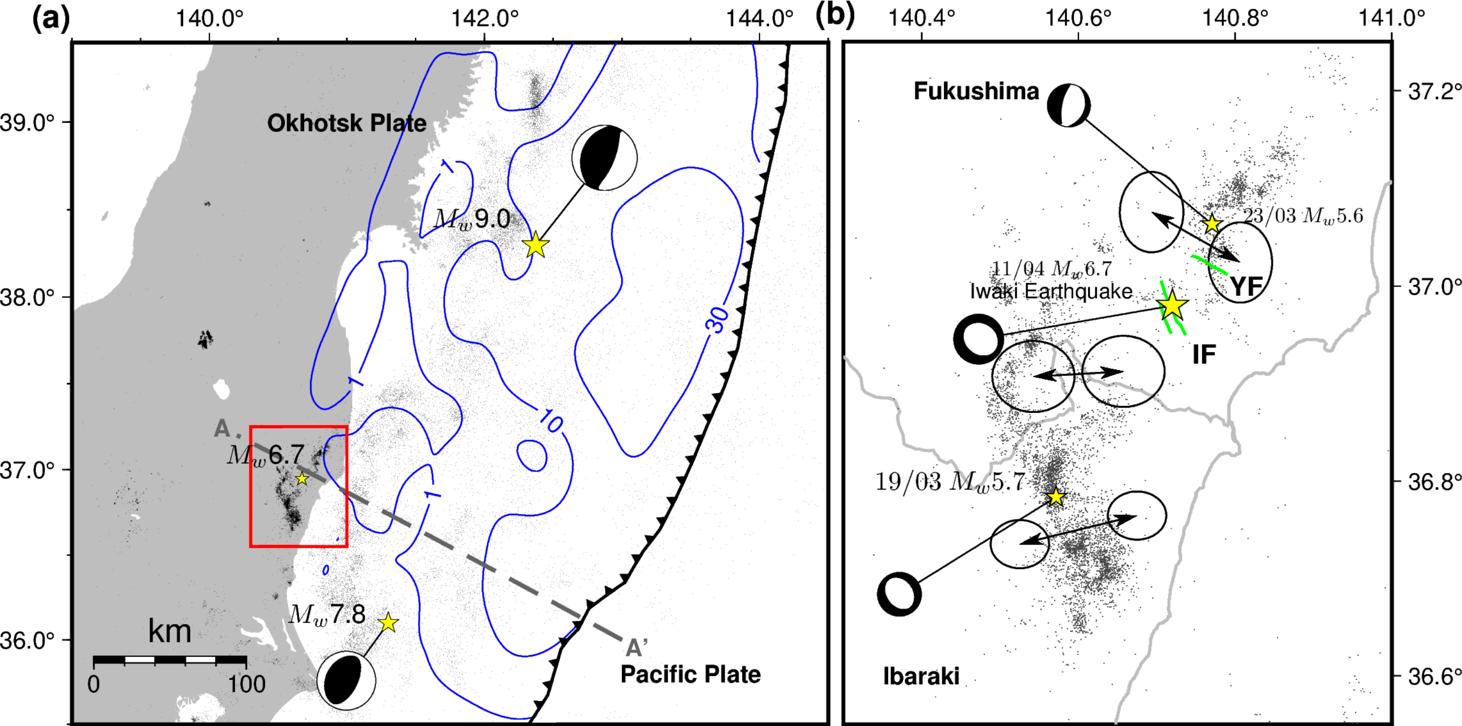

(a)
140.0°
142.0°
144.0°
39.0°
38.0°
37.0°
36.0°
Okhotsk Plate
$M_w$9.0
1
10
30
A
A'
$M_w$6.7
$M_w$7.8
km
0
100
Pacific Plate
(b)
140.4°
140.6°
140.8°
141.0°
37.2°
37.0°
36.8°
36.6°
Fukushima
23/03 $M_w$5.6
11/04 $M_w$6.7
Iwaki Earthquake
YF
IF
19/03 $M_w$5.7
Ibaraki

**Figure 2.**

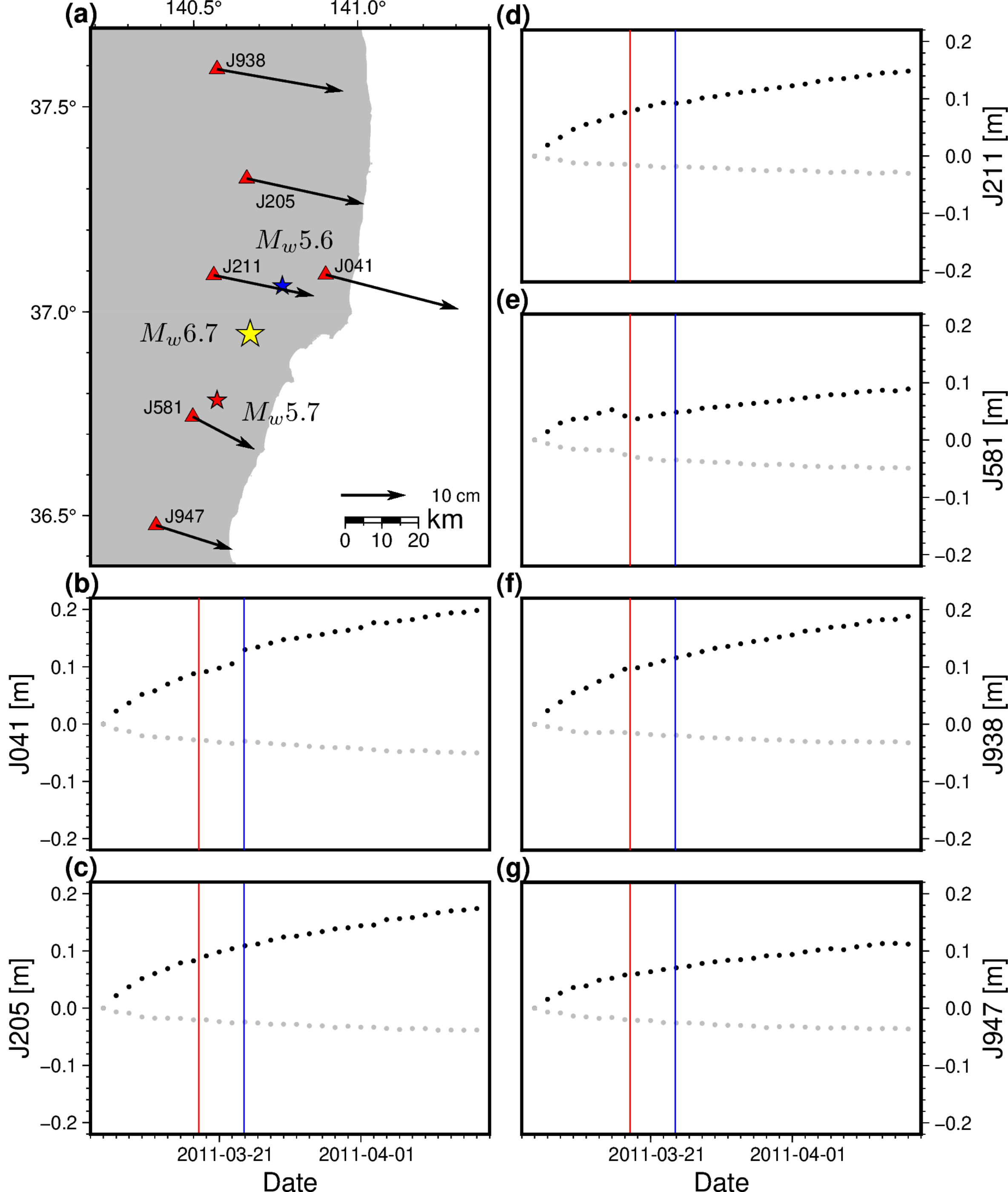

(a)
140.5°
141.0°
37.5°
37.0°
36.5°
J938
J205
$M_w5.6$
J211
J041
$M_w6.7$
J581
$M_w5.7$
J947
10 cm
km
0 10 20
(b)
J041 [m]
(c)
J205 [m]
(d)
J211 [m]
(e)
J581 [m]
(f)
J938 [m]
(g)
J947 [m]
0.2
0.1
0.0
−0.1
−0.2
2011-03-21
2011-04-01
Date

**Figure 3.**

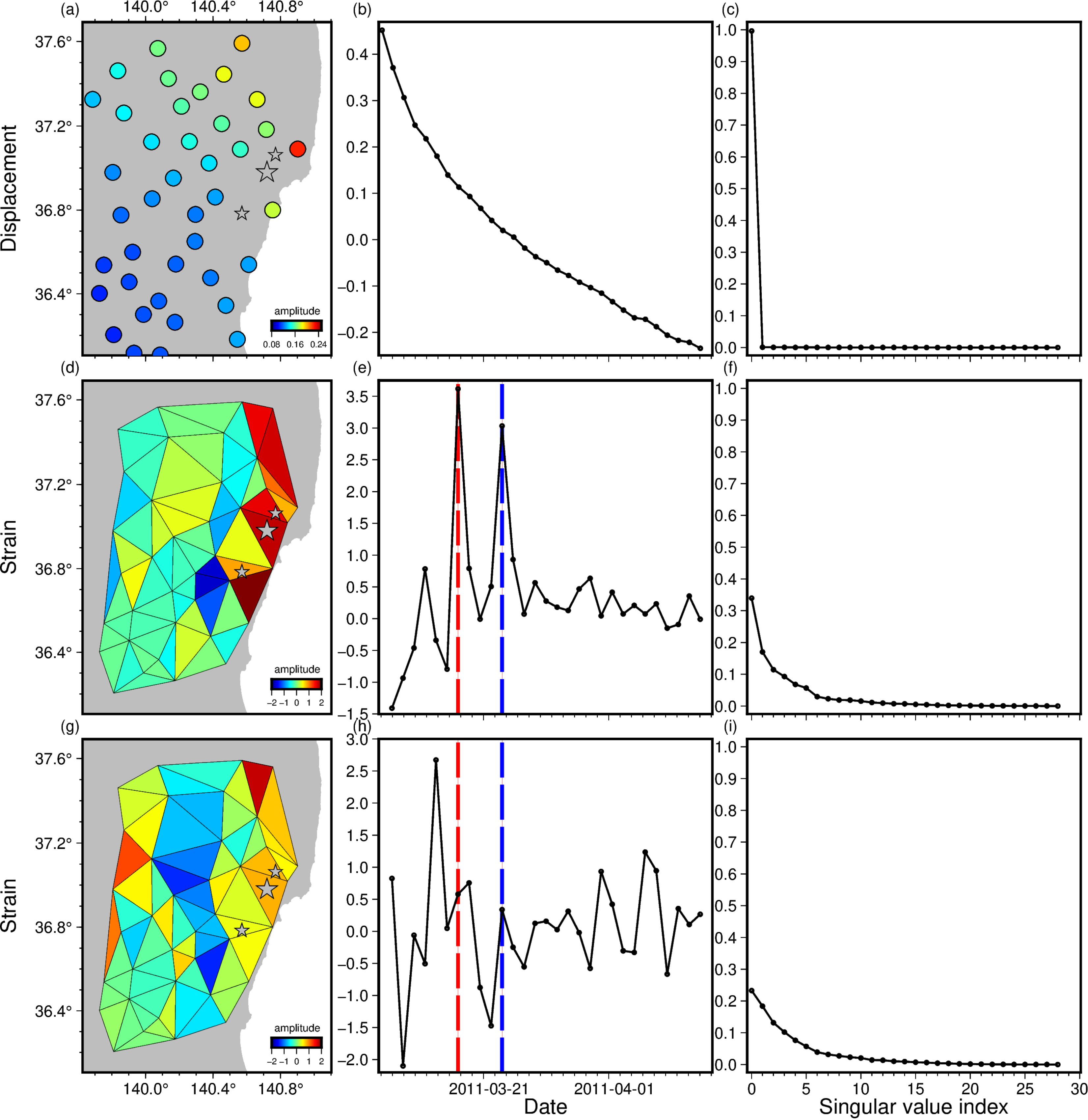

(a)
(b)
(c)
(d)
(e)
(f)
(g)
(h)
(i)
Displacement
Strain
Strain
amplitude
0.08 0.16 0.24
−2 −1 0 1 2
140.0° 140.4° 140.8°
37.6° 37.2° 36.8° 36.4°
2011-03-21
2011-04-01
Date
Singular value index

**Figure 4.**

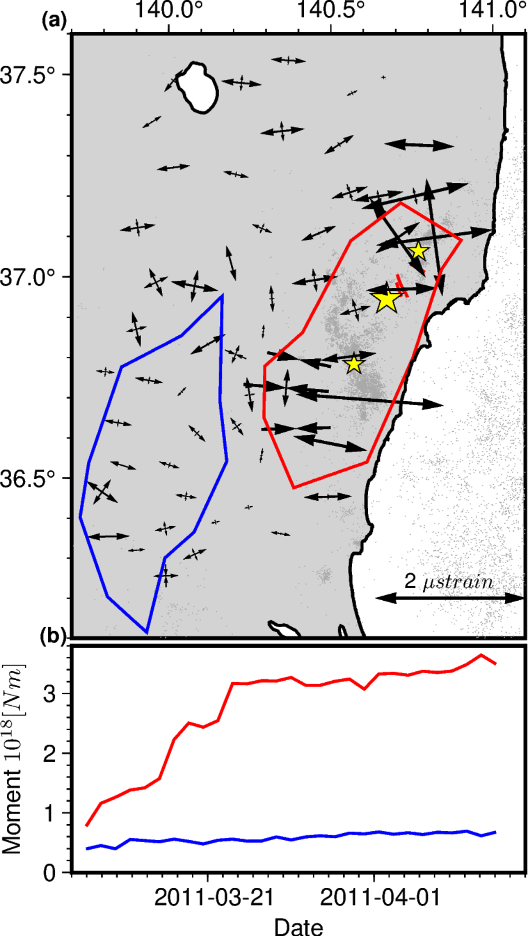

(a)
140.0°
140.5°
141.0°
37.5°
37.0°
36.5°
2 $\mu strain$
(b)
Moment $10^{18}[Nm]$
3
2
1
0
2011-03-21
2011-04-01
Date

**Figure 5.**

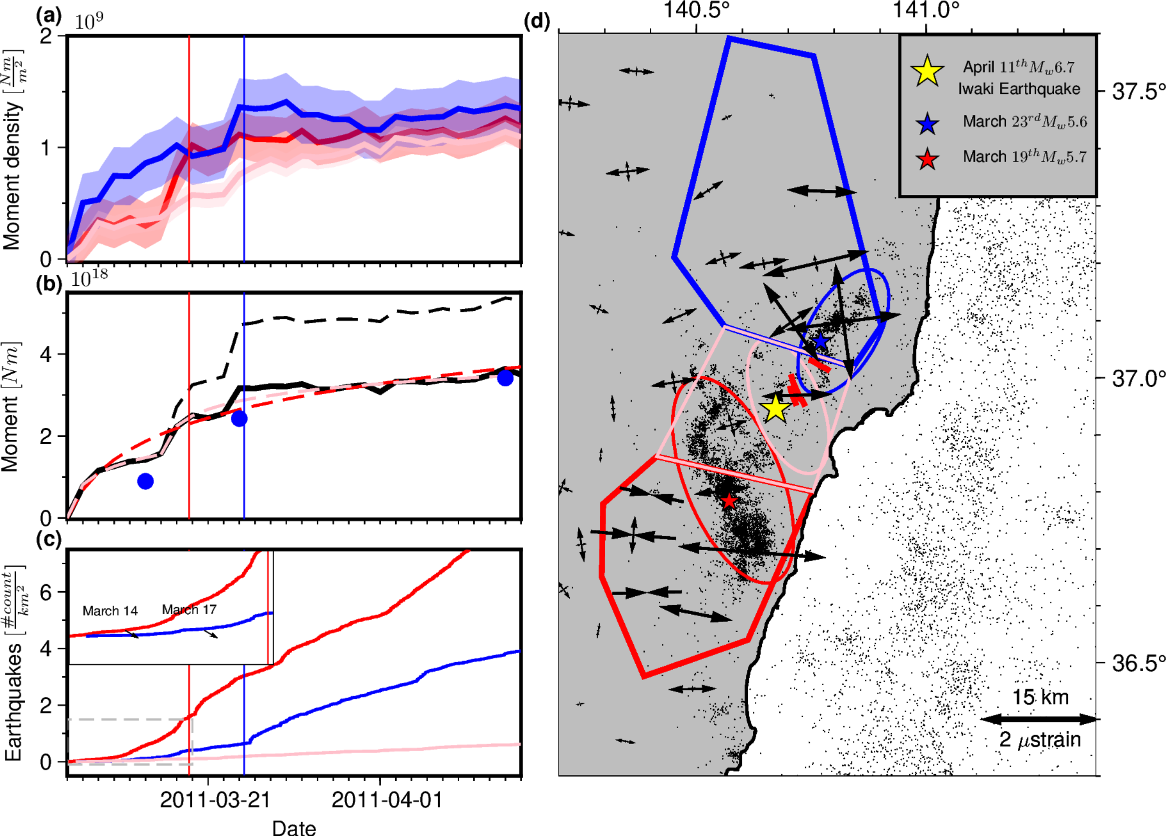

(a)
$10^9$
Moment density $[\frac{Nm}{m^2}]$
(b)
$10^{18}$
Moment $[Nm]$
(c)
Earthquakes $[\frac{\#count}{km^2}]$
March 14
March 17
2011-03-21
2011-04-01
Date
(d)
140.5°
141.0°
37.5°
37.0°
36.5°
April $11^{th}M_w6.7$
Iwaki Earthquake
March $23^{rd}M_w5.6$
March $19^{th}M_w5.7$
15 km
2 $\mu$strain

**Figure 6.**

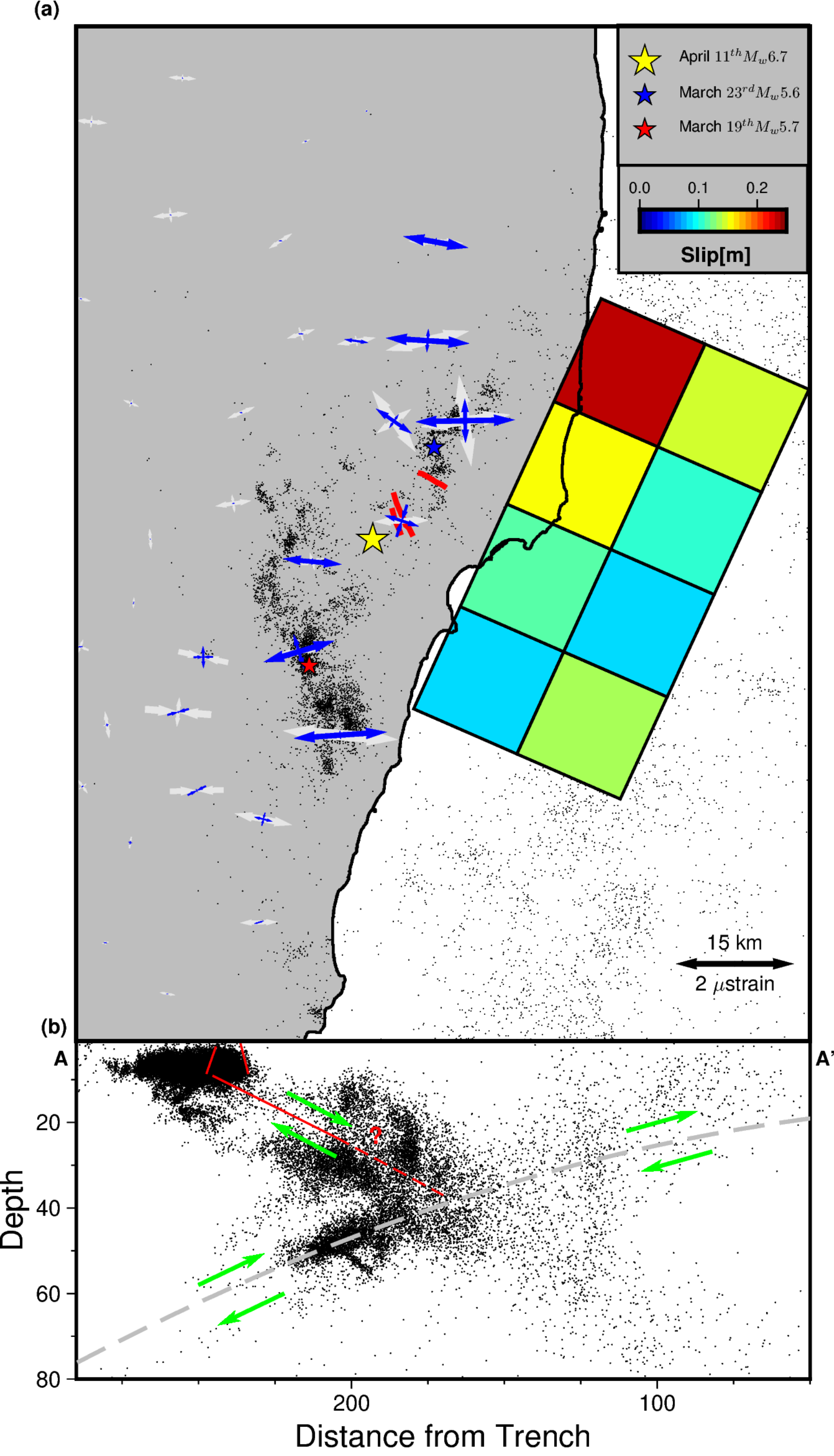
(a)
April $11^{th} M_w 6.7$
March $23^{rd} M_w 5.6$
March $19^{th} M_w 5.7$
0.0
0.1
0.2
Slip[m]
15 km
2 $\mu$strain
(b)
A
A'
?
20
40
60
80
Depth
200
100
Distance from Trench

**Figure 7.**

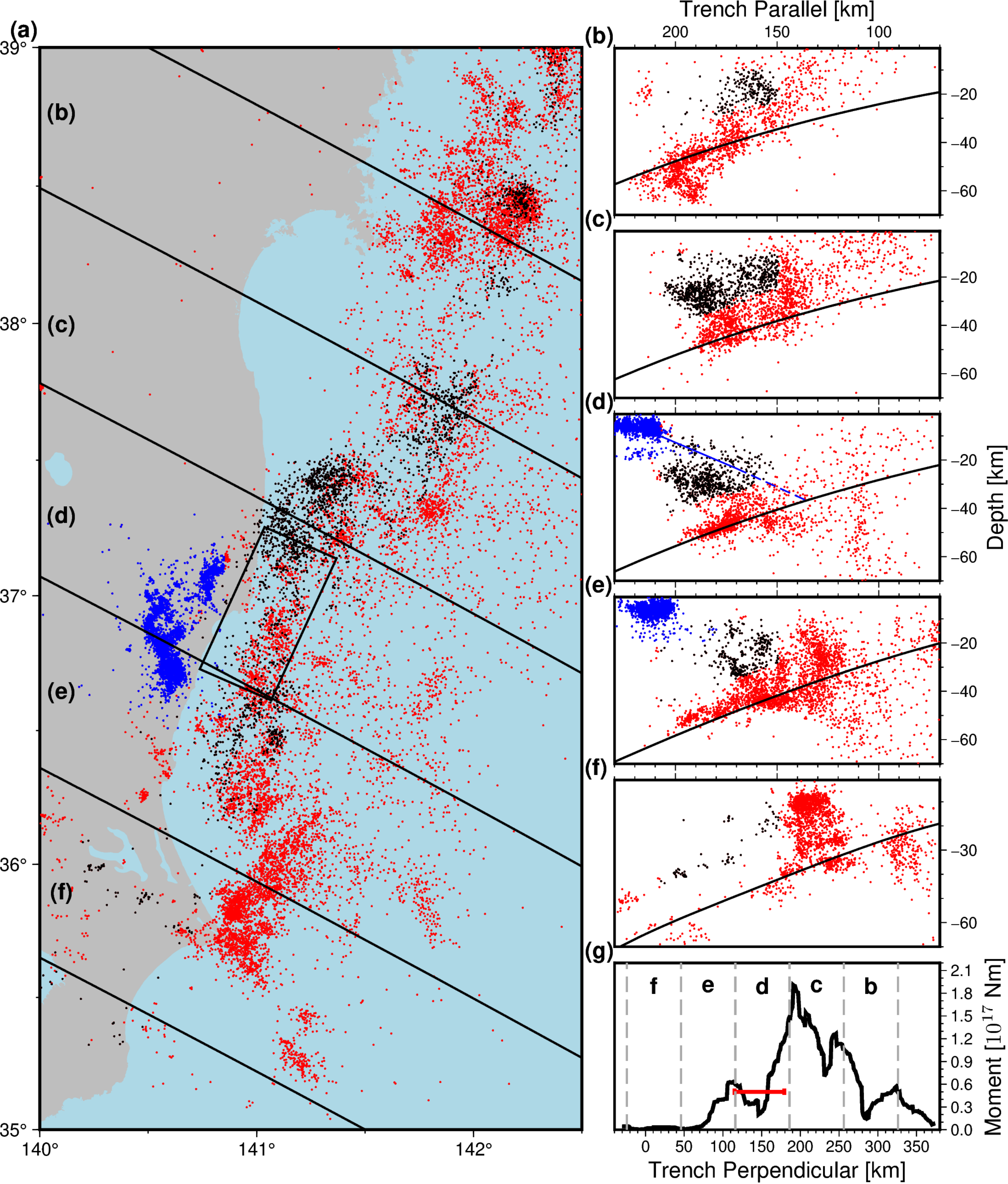

(a)
(b)
(c)
(d)
(e)
(f)
(g)
39°
38°
37°
36°
35°
140°
141°
142°
Trench Parallel [km]
200
150
100
Depth [km]
−20
−40
−60
−30
f
e
d
c
b
Moment [$10^{17}$ Nm]
2.1
1.8
1.5
1.2
0.9
0.6
0.3
0.0
0
50
100
150
200
250
300
350
Trench Perpendicular [km]

**Figure 8.**

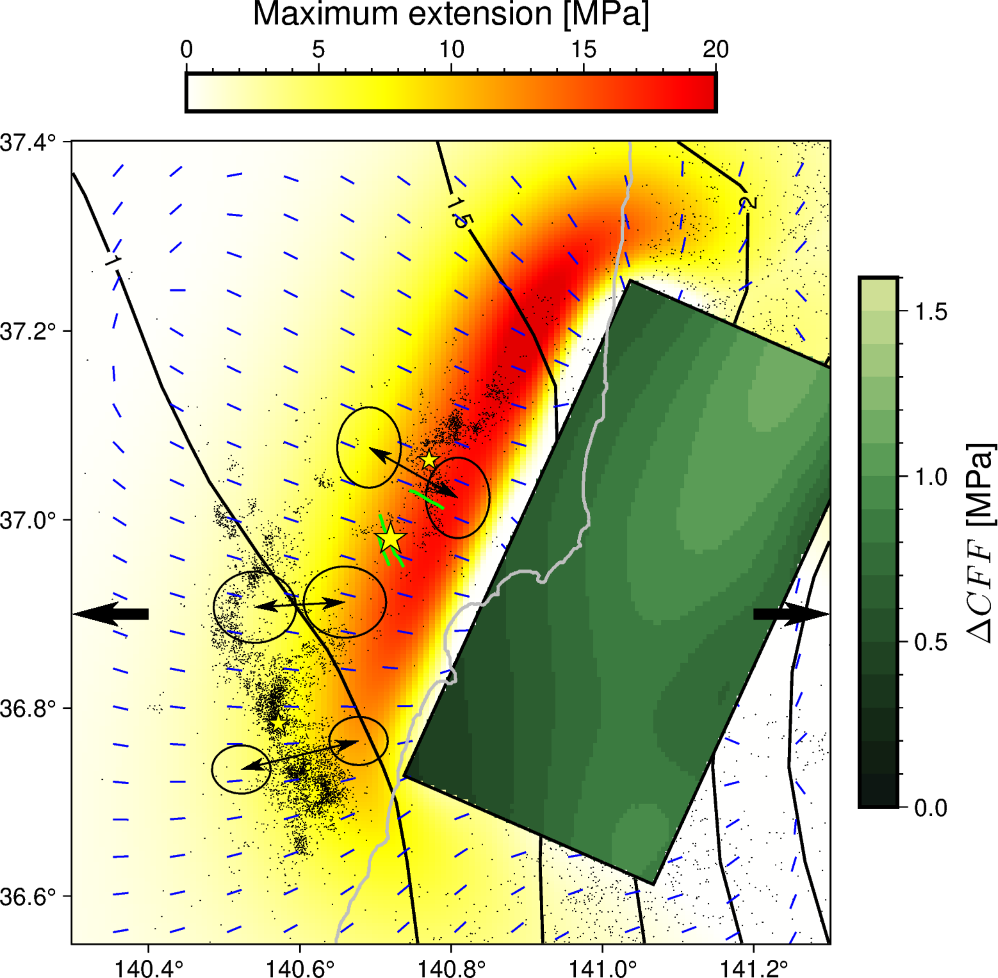

Maximum extension [MPa]
0
5
10
15
20
37.4°
37.2°
37.0°
36.8°
36.6°
140.4°
140.6°
140.8°
141.0°
141.2°
1
1.5
2
1.5
1.0
0.5
0.0
ΔCFF [MPa]

**Figure 9.**

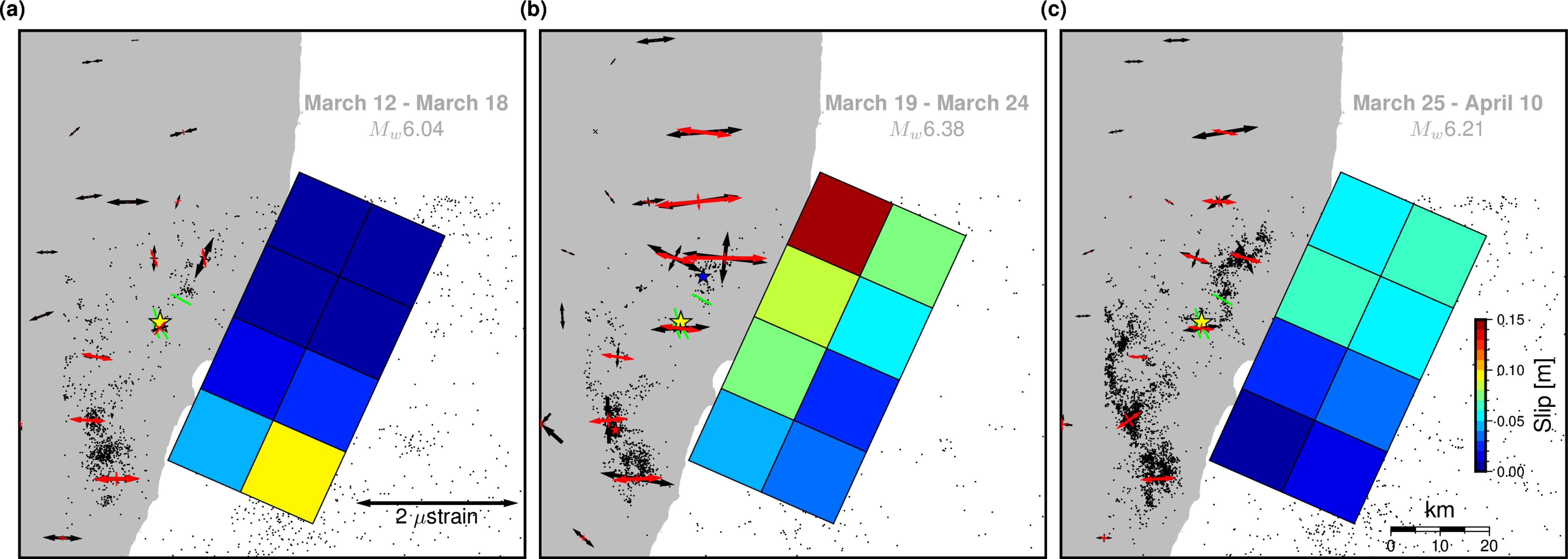

(a)
March 12 - March 18
$M_w$6.04
2 $\mu$strain
(b)
March 19 - March 24
$M_w$6.38
(c)
March 25 - April 10
$M_w$6.21
Slip [m]
0.15
0.10
0.05
0.00
km
0
10
20

**Figure 10.**

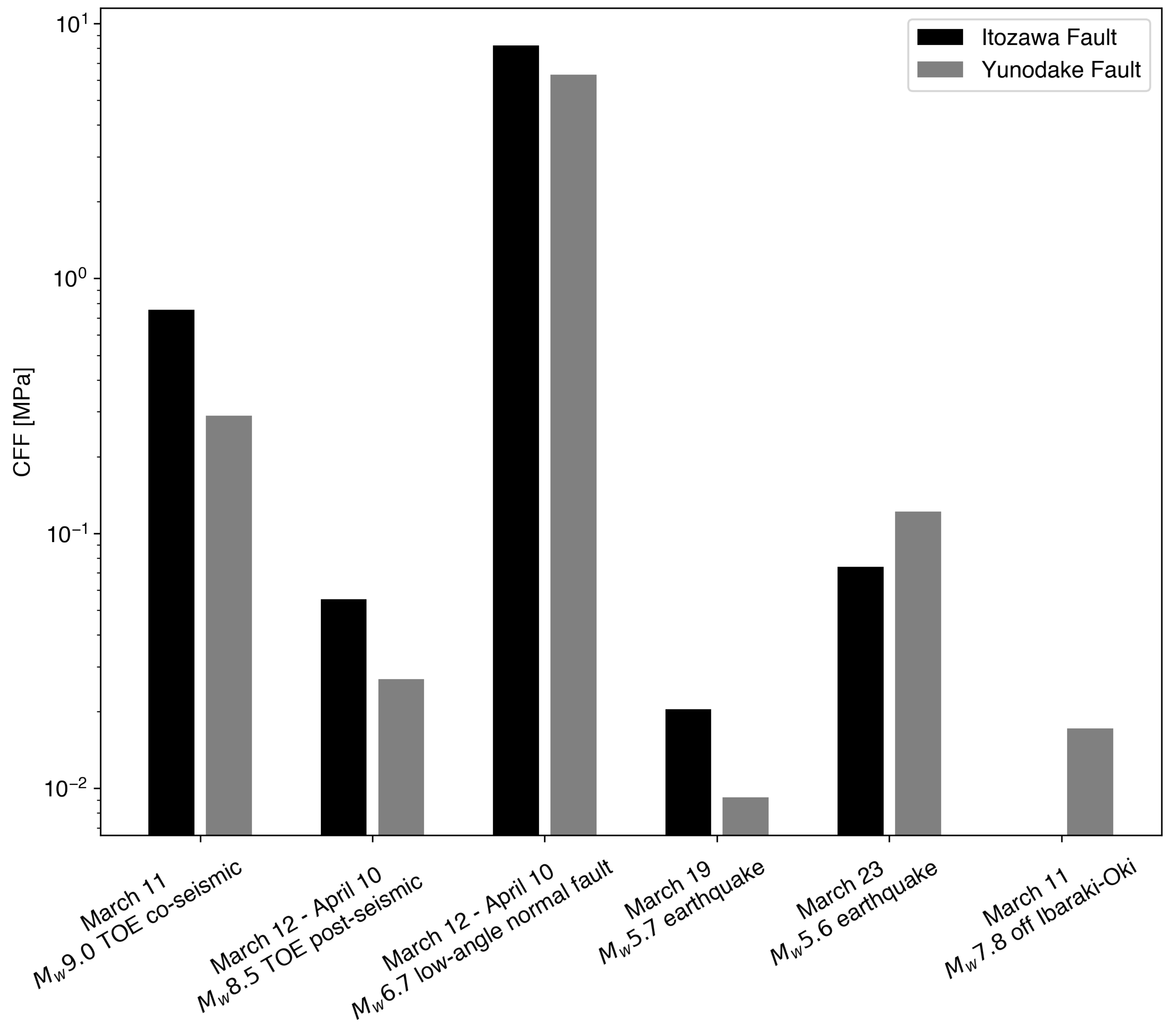

Itozawa Fault
Yunodake Fault
CFF [MPa]
$10^1$
$10^0$
$10^{-1}$
$10^{-2}$
March 11
$M_w$9.0 TOE co-seismic
March 12 - April 10
$M_w$8.5 TOE post-seismic
March 12 - April 10
$M_w$6.7 low-angle normal fault
March 19
$M_w$5.7 earthquake
March 23
$M_w$5.6 earthquake
March 11
$M_w$7.8 off Ibaraki-Oki